Title
Advanced Braking Methods for Longitudinal Control of Commercial Heavy Vehicles

Authors
Moklegaard, Lasse
Stefanopoulou, Anna G.

Publication Date
2000-07-01

This paper uses Postscript Type 3 fonts. Although reading it on the screen is difficult it will print out just fine.

CALIFORNIA PATH PROGRAM
INSTITUTE OF TRANSPORTATION STUDIES
UNIVERSITY OF CALIFORNIA, BERKELEY

Advanced Braking Methods for Longitudinal Control of Commercial Heavy Vehicles

Lasse Moklegaard, Anna G. Stefanopoulou
University of California, Santa Barbara

California PATH Research Report
UCB-ITS-PRR-2000-8

This work was performed as part of the California PATH Program of the University of California, in cooperation with the State of California Business, Transportation, and Housing Agency, Department of Transportation; and the United States Department of Transportation, Federal Highway Administration.

Report for MOU 372

May 2000

ISSN 1055-1425

Advanced Braking Methods for Longitudinal Control of Commercial Heavy Vehicles

Lasse Moklegaard
Anna G. Stefanopoulou

Department of Mechanical and Environmental Engineering
University of California, Santa Barbara
Santa Barbara, CA 93106-5070

MOU 372

PATH Research Report

This work was performed as part of the California PATH Program of the University of California, in cooperation with the State of California Business, Transportation, and Housing Agency, Department of Transportation; and the United States Department of Transportation, Federal Highway Administration.

January 2000

Advanced Braking Methods for Longitudinal Control of Commercial Heavy Vehicles

Lasse Moklegaard and Anna G. Stefanopoulou
January 2000

Abstract

In this report, we develop nonlinear dynamical models and longitudinal control algorithms that coordinate a variable compression brake mechanics with service brakes for a Class-8 commercial heavy vehicle (CHV). For the coordination and full use of these retarding actuators, we first model the multivariable system based on first principles and experiment data. A nonlinear crank angle based model is first developed for the novel variable compression brake actuator. A family of linear reduced order models is also identified and used for control analysis and development.

Moreover, a sensitivity analysis and an evaluation of the model variations across operating regimes, allow us to formulate the control problem and to assess the difficulties in the control design. The challenges in the control design are summarized as: mode switching, large parameter variations, control authority allocation, and saturation of redundant actuators.

In the last part of this report, we design a coordinated braking controller that combines a high priority PI-controller for the compression brake with a P-controller for the service brakes. The priority of the controllers is scheduled based on the saturation of the compression brake. Simulation results show that the variable compression brake allows smooth and fast speed regulation, and rejection of torque disturbances due to changes in the road grade.

We also establish two measures that quantify the benefits of the developed semi-autonomous, coordinated braking system compared to manually using the service brakes alone. One measure is related to the settling time for the system, and it addresses safety. The other measure is related to the use of service brakes and addresses maintenance cost. We show that, for one specific critical braking maneuver, the coordination of compression and service brakes reduces the use of the service brakes by a factor of 2, and that it reduces the settling time by a factor of 45.

Keywords

Advanced Vehicle Control Systems
Brakes
Commercial Vehicle Operations
Speed Control

Executive Summary

In this report, we summarize our work on longitudinal control of commercial heavy vehicles (CHVs) equipped with novel retarding actuators. CHVs are an essential part of our nation's economy, and an efficient link between marine, railroad and air transportation nodes. Increased highway speed and transportation demands, coupled with limitations in traditional service brake actuators (friction pads on the wheels) create a challenging control problem that requires additional retarding actuators and coordination with service brakes. Although, service brakes can theoretically provide a retarding power ten times higher than the accelerating power of the vehicle, they cannot be used continuously because of the generated heat and associated wear of the friction contacts. The presence of delays associated with the pneumatic or the hydraulic actuation subsystem, impose additional constrains on the longitudinal control of CHVs. Faced with these difficulties, fleet and engine manufacturers are introducing additional retarding mechanisms, wherein the most innovative, powerful, and complex one is the compression brake.

The research accomplishments of our work are as follows. We develop nonlinear dynamical models and preliminary control algorithms for a Class-8 CHV, equipped with a compression brake mechanism. Two types of models are developed. First, a detailed crank angle based engine model is developed. This high order model describes the intrinsic transient interactions between individual cylinder intake and exhaust gas processes, turbocharger dynamics, and vehicle dynamics during combustion and variable compression braking. The model is validated using quasi-static experimental data. Second, a family of low-order models appropriate for control analysis and design is developed using signal processing, and input-output identification techniques. Moreover, a sensitivity analysis and an evaluation of the model variations and uncertainties across operating regimes, allow us to formulate the control problem and to assess the difficulties in the control design. In particular, we show that there is a significant sensitivity to changes in the gear ratios, in fact, the time constant for the system varies from 22 seconds when using the first gear, to about 142 seconds when using the tenth gear. This is a variation of more than 640 percent. Variations in the vehicle mass also greatly influence the vehicle dynamics. The mass for the system can vary as much as 400 percent from being tractor only, to being a system of tractor and trailer(s) with maximum allowable load. Even during nominal operating conditions, the controller is required to operate in three distinct modes: combustion, braking, and transition. Each mode is governed by very different dynamics.

In the last part of this report, an initial low order controller is designed for the linear reduced order model. Specifically, we design a high priority PI-controller for the compression brake, combined with a P-controller for the service brakes. The priority of the controllers is scheduled based on the saturation of the compression brake. Nonlinear simulations are used to assess the closed-loop performance. The results show that the variable compression brake allows smooth and fast speed regulation and rejection of torque disturbances due to changes in the road grade.

To quantify the benefits of the developed semi-autonomous, coordinated braking system compared to manually using the service brakes alone, we establish two measures: one that is based on settling time and addresses safety, and one that is related to the use of service brakes and addresses maintenance cost. We show that for one specific critical braking maneuver the coordination of the brakes reduces the use of the service brakes by a factor of 2, and that it reduces the settling time by a factor of 45.

The challenges in the control design are summarized as: mode switching, large parameter variations, control authority allocation, and saturation of redundant actuators.

Contents

1 Introduction

Commercial heavy vehicles ($CHVs$) are an essential part of our nation's economy, and an efficient link between marine, railroad and air transportation nodes. In 1996, the intercity trucking industry accounted for $176.8 billion in revenues and over 2.9 million jobs [13].

Over the last ten years, there has been a significant improvement of the reliability and efficiency of the CHV powertrain. This transformation is primarily achieved by using lightweight material, and by reducing the aerodynamic drag and frictional losses. It is evident, however, that as fuel efficiency increases, the natural braking capability of the CHV decreases. In addition to natural limitations of the braking power, the air brake system on a tractor-semitrailer vehicle introduces a considerable delay during the actuation phase. Also, due to the large mass of a CHV, the air brakes are already operating close to the pressure limit. This can potentially lead to problems during combined longitudinal and lateral controller operation, as described in the following scenario, adapted from [14]: Consider the case where the tractor-trailer vehicle has to decelerate while negotiating a tight turn. To prevent the potential of jack-knifing (a large, uncontrolled relative jaw motion between the tractor and trailer) the lateral controller wants to activate its differential braking feature on the rear trailer brakes, but cannot do it because the outside trailer brake is already saturated by the longitudinal controller. If the longitudinal controller, however, was able to use an auxiliary retarder, such as the compression brake, a decision to choose between the lateral or the longitudinal control objectives would not be necessary.

In Automated Highway Systems (AHS), the major goals are to increase highway capacity and to enhance driving safety by automatic longitudinal and lateral control of vehicles [22]. It is clear, however that braking power and braking control impose fundamental limitations in achieving these goals. The long term objectives of this project are, therefore, to increase retarding power to accommodate the wish for higher operating speed, to lower maintenance cost on service brakes by coordinating service and engine brakes, and to enhance safety during critical lateral maneuvers, by coordinating vehicle retarders with the steering mechanism.

The organization of this report is as follows. In Section 2, we review the work that has been done on related research. Section 3 contains descriptions of two potential vehicle retarders in addition to the compression brake. We develop a longitudinal vehicle model in Section 4, in addition to examine the current compression brake technology. The engine modeling work is described in Section 5. In a sub-section here, we conduct numerical model order reductions of the nonlinear engine dynamics. The result is a family of low-order, linear models appropriate for control analysis and design. In Section 6, we validate the modeling work by comparing model prediction with measured data. The control formulation is stated in Section 7, while linearization, sensitivity analysis, preliminary control design, and simulation results are located in Section 8. Section 9 contains concluding remarks, and pointers to future work.

2 Background

Over the past few years, there has been an increased activity on state, national, and international level, on safety related issues for CHVs. Because of this, there is a concentrated research effort going on in the industrial, governmental, and in the academic community.

The need for brake power is addressed by truck manufacturers and fleet managers by the development of various retarding mechanisms in addition to the service brakes (drum or disc brakes on the vehicle wheel). The main categories of these retarders are engine brakes and shaft brakes. In the first category, compression brakes enhance braking efficiency by modifying the conventional gas exchange process. In the second category, shaft retarders are devices attached to the transmission, driveline, or axle that use high turbulence or electro-magnetic forces to dissipate the rotational energy of the moving parts.

None of these decelerating actuators are supporting fully automatic operation and depend significantly on well trained drivers. It is important to note here that none of these retarding actuators, typically used in Class 7-8 vehicles, have been integrated into a unifying automatic retarding system. Integrated schemes of an electric driveline retarding mechanism with advanced braking systems (ABS) and advanced traction systems (ATS) can only be found in hybrid-electric experimental vehicles [5].

All engine manufacturers are striving for variable compression brake effort. Work can be summarized by Jacobs variable brake valve timing [10], Cummins' discrete cylinder brake valve actuator [24], and Volvo's variable exhaust throttle actuator [2].

Related work on longitudinal control of CHVs is shown in [28], [26], [29], and [27], while initial results on the coordination of steering and braking is shown in [3]. In [28], control-oriented simulation models of heavy-duty vehicle, including diesel engine dynamics complete with turbocharger, intercooler, and automatic transmission with torque converter are developed. Using these models, several longitudinal controllers for automated CHVs that can operate reliably and yield good performance, both with and without intervehicle communication, are developed in [27]. One of the most critical obstacles in automated operation of CHVs is the presence of significant delays in the fuel and brake actuators. These delays are particularly important in longitudinal control of platoons without intervehicle communication. The effect of the actuator delays cumulate as they propagate upstream, and the result is performance degradation. In [26], and [29], backstepping-based nonlinear controllers and a PID-based nonlinear controller are developed. These controllers recover, on the expense of higher controller complexity, the original performance of the system without the actuator delays.

One of the most common causes of highway accidents involving CHVs is the uncontrolled, large relative yaw motion between the tractor and the trailer, commonly refereed to as jack-knifing. In [3], a lateral controller which independently control the braking force on the outer and inner rear trailer wheels is developed. This independent braking system is activated when the relative articulation angle between the tractor and trailer exceeds an upper limit. To meet lateral lane follow objectives, this independent braking control scheme is coordinated by the front wheel steering mechanism [3].

3 Auxiliary Retarding Actuators

Although, we will concentrate on the compression brake mechanism in this report, we briefly discuss two other commonly used retarding actuators.

3.1 Driveline Retarder

Hydraulic driveline retarders are based on the principal of hydraulic coupling and resistance between a rotor attached to the crankshaft or driveline of the vehicle, and the fins of a stator. Caterpillar and Voith develop a manual and automated mechanism that allow modulated or full braking power, respectively. The mechanism enables smooth and somewhat controlled braking effort at non-zero rotational speed. Allison driveline retarders can apply braking power directly to the driveline and is, therefore, used for stop-and-go driving conditions typical for buses in intercity operation.

Electric driveline retarders by Jacobs and Rockwell International, on the other hand, are typically based on dissipating kinetic energy from the driveline by means of setting up a magnetic field. This mechanism is, currently, the only one that allows integration with ABS and ATS.

3.2 Exhaust Brake

Exhaust braking is based on an add-on device that restrict the flow out of the exhaust manifold. The result is an increase in the exhaust pressure, which in turn decreases the output power of the engine. The exhaust brake is easy to install, but does not provide high retarding capabilities. Jacobs and Pacific Diesel Brake manufacture this device.

Figure 1: **Left:** Driveline retarder (Source: [25]). **Right:** Exhaust brake (Source: [1]).

3.3 Compression Brake

Compression braking is based on inhibiting fuel injection, altering the existing exhaust valve opening, and thereby converting the engine into a compressor. At the end of the compression stroke, close to when fuel injection usually takes place, the exhaust valve opens, and the compressed air is released into the exhaust manifold.

We call this secondary opening of the exhaust valve the braking event, and the corresponding valve timing for brake valve timing, v_{eb}. The exhaust valve lift profile is considerably different for the two different events, as shown in Figure 2. For simplicity,

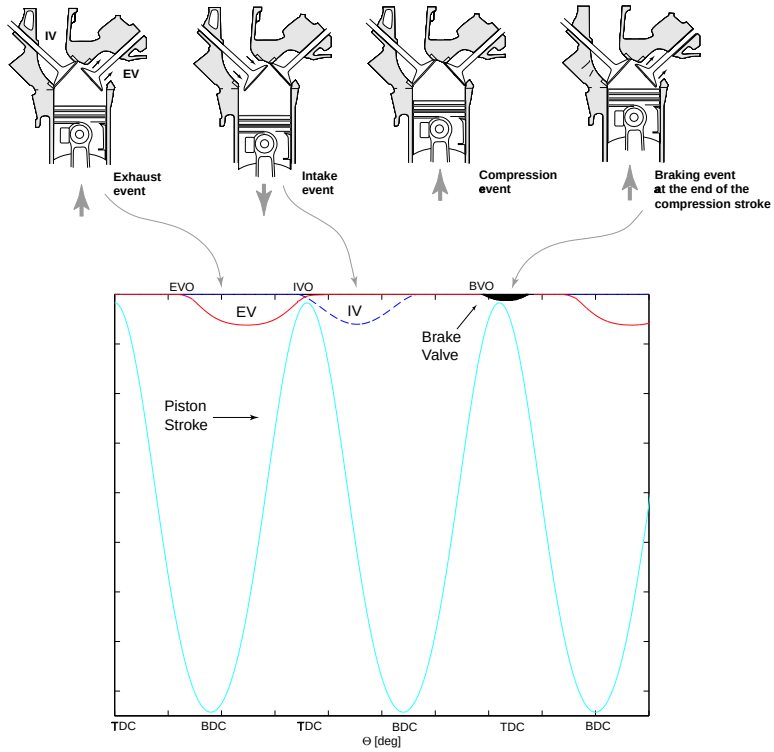

Figure 2: Schematic drawing and traces of piston motion and valve lift profiles.

we call the braking-event profile of the exhaust valve the "brake valve". The activation of the brake valve is typically achieved through a master-slave hydraulic system. The exact profile and timing for the brake valve are designed to maximize the braking power, i.e., to generate the highest peak cylinder pressure. The brake valve profile needs to satisfy constraints on component loading due to high in-cylinder pressure, and geometric clearance between the brake valve trajectory and the piston motion. It is this type of actuator we are focusing on in this project.

Figure 3, on the other hand, illustrates the valve timing events plotted in a **PV**[1] diagram. This diagram shows the engine operation during conventional 4-stroke cycle operation (dotted line) and the 4-stroke cycle operation during compression braking (solid line). It is generated using outputs from the model developed in Section 5, during steady-state engine conditions. Note here that steady-state conditions are defined in a cycle-averaged sense. The engine is considered at steady-state even though its crank angle based behavior is periodic with one firing or braking cycle as the period. In the **PV** diagram, the piston work is positive during combustion and negative during braking. Thus, compression brake is a retarding mechanism that is achieved by inhibiting fuel injection and the combustion event, and, thereby, transforming the engine into a compressor. In that mode, the engine acts like a energy sink [4], because the crankshaft kinetic energy is used to compress the air during the

[1] **PV** diagram is the plot of cylinder pressure vs. cylinder volume. It is used in the engine deign and thermodynamic communities extensively, since the line integral represents work: $W = \oint p_{cyl} dV_{cyl}$

compression stroke. Close to top-dead-center (TDC), the compressed air is released to the exhaust manifold.

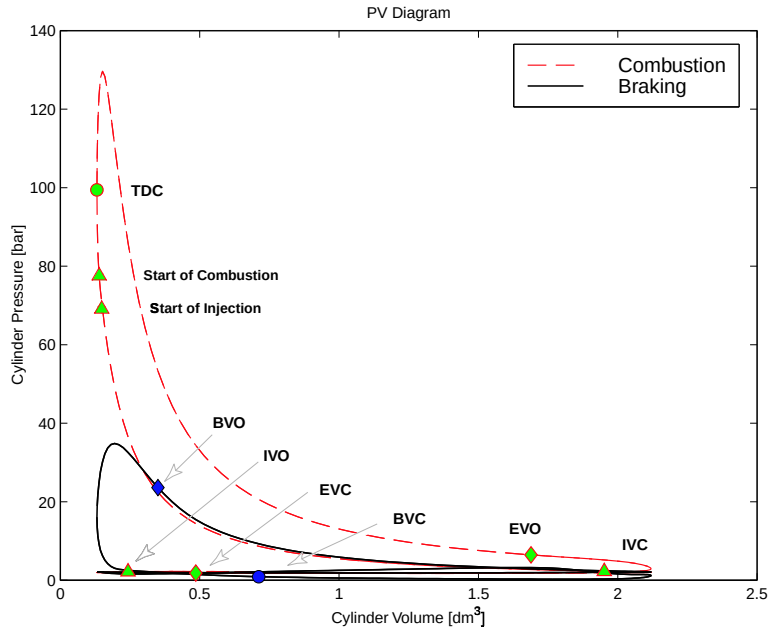

Figure 3: Cylinder pressure versus cylinder volume during combustion (dashed), and braking mode (solid).

4 Longitudinal Vehicle Model

A lumped parameter approximation of the vehicle rotational dynamics shown in Figure 4 can be used to describe the longitudinal dynamics for a vehicle with rotational engine speed, ω_e, mass, M, and engine inertia, J_e.

$$J_T \frac{d\omega_e}{dt} = TQ_{eb} + r_g(F_\beta - F_{sb} - F_a - F_r), \quad (1)$$

where

$$\begin{array}{rcll} F_\beta & = & -Mg\sin(\beta), & \text{gravitational force due to grade} \\ F_r & = & -\mu Mg\cos(\beta), & \text{rolling resistance} \\ F_a & = & \frac{\rho C_d A_v}{2}(r_g\omega_e)^2, & \text{aerodynamic force} \\ J_t & = & (M + \frac{J_e}{r_w^2})r_g^2, & \text{total inertia} \\ r_g & = & \frac{r_w}{g_t g_{fd}}, & \text{total gear ratio} \\ TQ_{eb} & = & f_1(\omega_e, v_{eb}), & \text{engine torque (identified in Section 5.2)} \\ F_{sb} & = & f_2(v_{sb}), & \text{wheel force due to service brake (identified in Section 4.1).} \end{array}$$

The gravitational force due to the grade, β, is denoted by F_β. The rolling resistance force, F_r, depends on both the grade, β and the rolling resistance, μ. The aerodynamic force, F_a, depends on the drag coefficient, C_D, the frontal are, A and the air density, ρ. The total vehicle inertia reflected to the engine shaft, J_T, depends on the vehicle mass, M, and the total gear ratio, r_g. The gear ratio depends on the wheel diameter, r_w, and the transmission and final drive gear ratio, g_t, and g_{fd}, respectively. Note that the wheel rotational speed has the following relation to the engine speed: $\omega_w = \frac{r_g}{r_w}\omega_e$. TQ_{eb} is the engine shaft torque during compression braking, while F_{sb} is the service brake force applied to the wheel rim. The dynamical equations describing F_{sb} and TQ_{eb} are discussed in detail below.

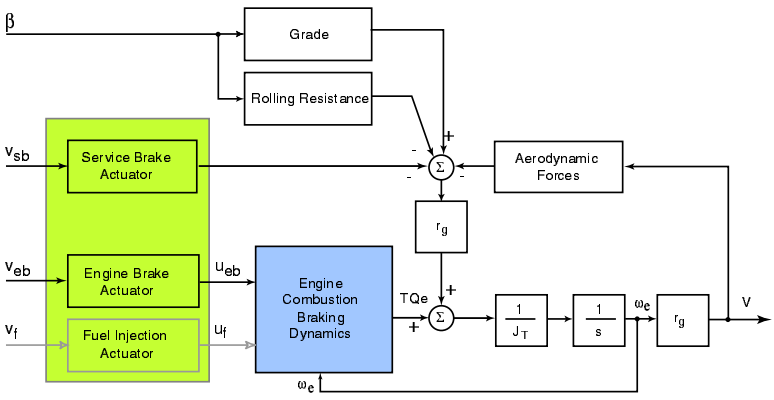

Figure 4: Open-loop block diagram of the vehicle model.

4.1 Service Brakes

The conventional service brake force on the wheel can be modeled using a static nonlinear function, a first order differential equation with a time constant, τ_{sb}, and a delay, t_{sb}. The static nonlinear function is a function of the applied pedal force,

or simpler, the pedal displacement, v_{sb}, (for details see [29, 18, 7]). τ_{sb} and t_{sb} are nonlinear and uncertain functions of temperature and brake conditions.

$$\frac{dF_{sb}}{dt}(t+t_{sb}) = \frac{1}{\tau_{sb}}(F^*_{sb} - F_{sb}(t+t_{sb})) \quad (2)$$

$$F^*_{sb} = f_{sb}(v_{sb}). \quad (3)$$

It is well known that the service brakes have weak DC authority because of overheating. The current practice of "snubbing" the service brake (application of high pressure pulses) rather than "dragging" (application of a constant low pressure) exemplifies their low DC authority [6].

4.2 Compression Brake

The additional retarding power from the compression brake is used during severe deceleration commands in highway maneuvers. The compression brake is typically used in on-off fashion, but there is no prior work done on identifying DC components or on identifying the dynamics for this actuator. Although, the service brakes have large retarding authority, they cannot be used in continuous mode because of overheating. The compression brake, on the other hand, can be used continuously due to the heat dissipation through the engine cooling system. Identifying the bandwidth of the compression brake on different engine and drivetrain operating conditions requires a detailed crank angle based engine model. The goal of our modeling work in Section 5, is to identify the nonlinear dynamics of the compression brake. Let x_{eb} be the state vector of the nonlinear dynamics, and $[\omega_e, v_{eb}]^T$ the input vector. The compression brake torque can then be described by:

$$\dot{x}_{eb} = f_{eb}(x_{eb}, \omega_e, v_{eb}) \quad (4)$$

$$TQ_{eb} = h_{eb}(x_{eb}, \omega_e, v_{eb}) \quad (5)$$

4.3 Torque versus Power

In the preceding sections, we developed a longitudinal vehicle model based on summation of torque on the engine shaft, given by Newton's laws. In the transportation community, however, the general practice is to use power rather than torque in equations and figures describing vehicle dynamics. The well-known relation between power and torque is given below:

$$P = TQ\,\omega, \quad (6)$$

where P is the power in W, TQ is torque in Nm, and ω is rotational speed in rad/sec. The longitudinal vehicle model expressed in terms of power contributions is then given by the following expression:

$$\frac{d\omega_w}{dt} = \frac{1}{J_T\omega_w}\left(P_{eb}(u_{eb}, \omega_w) - P_{sb}(u_{sb}) - P_a(\omega_w) + P_\beta(\beta) - P_r(\beta)\right) \quad (7)$$

4.4 Equilibrium Analysis

At equilibrium, the rate of change in vehicle speed is zero, and the power generated by the gravitational force during a grade descend is equal to the power dissipated by the engine retarding mechanisms. At equilibrium wheel speed, ω_w^*, Equation 7 is:

$$P_\beta = P_{eb} + P_{sb} + P_0, \tag{8}$$

where P_β is the gravitational power generated when the vehicle descend on a grade , β, and P_{eb} is the power *generated* by the engine if it is in combustion mode, otherwise it is the power *dissipated* by the engine if it is in braking mode. P_{sb} is the power dissipated by the service brakes, while $P_0 = -(P_a + P_r)$ is the natural braking power due to aerodynamic drag and rolling resistance, as they are defined in Equation 2, in Section 4.

The grade power, P_β, is linearly dependent on wheel speed, as seen in the following equation:

$$P_\beta = -Mg\sin(\beta)\omega_e = -Mg\sin(\beta)\frac{\omega_w}{r_g} \tag{9}$$

The power dissipated by the compression brake, P_{eb}, is derived in Section 5.3, Equation 44, and it is found to have the following quadratic speed form:

$$P_{eb} = \gamma_0\omega_w + \gamma_1 v_{eb}\omega_w + \gamma_2 v_{eb}^2 + \gamma_3\omega_w^2 + \gamma_4 v_{eb}\omega_w^2 \tag{10}$$

Figure 5 shows the grade power, P_β and P_{eb} together with the natural braking power, P_0, as functions of wheel speed, ω_w. Figure 5 is very informative and it

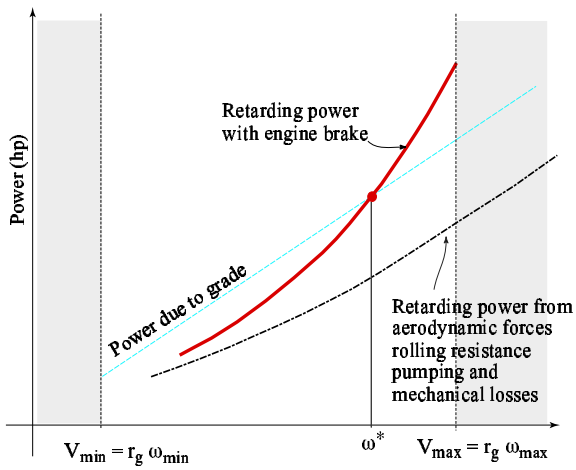

Figure 5: Vehicle speed versus braking power during a steep descent.

is extensively used in the actuator component design, but it does not provide any information about the system transient behavior. The brake valve timing affects both the maximum braking effort and the speed at which this maximum effort is achieved. The delays and time constants of the brake actuators, coupled with the dynamic response of the turbocharged engine, can impose severe limitations on the stability of the vehicle velocity. Nowadays, these limitations are primarily treated by the predictive action of trained drivers. Identifying the bandwidth of the compression brake on different engine and drivetrain operating conditions is important for the design of safer and faster heavy commercial vehicles.

4.5 Past and Present set of Equilibrium Points

It is of interest to see how the compression brake technology has evolved since 1966 when it first was introduced to the transportation industry in a 1966 SAE paper by Cummins [4]. Figure 6 shows how the equilibrium point that defines the vehicle descending speed has changed from 1966, ω_{w66} to 1999, ω_{w99}. The data for the curve denoted as "Engine Brake, 1966," is adapted from [4]. First of all, the current descending wheel speed is higher than the one attained in 1966, $\omega_{w99} > \omega_{w66}$. It is important to note that ω_{w99} is a *stable* equilibrium point, while ω_{w66} is *unstable*. The reasons for this change in stability are two folded: for low speed, there has been a big improvement in the reduction of mechanical losses, such as friction, pumping losses and aerodynamic drag. This improvement is due to an increasing demand for better fuel economy and reduction in emissions. For high speed, on the other hand, the increase in braking power is most likely due to improvements in the actuator components. The combination of these improvements result in a higher, and stable equilibrium, ω_{w99}.

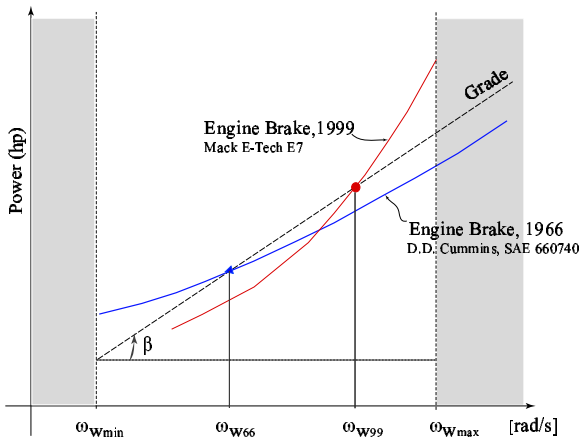

Figure 6: Figure show how the equilibrium point has changed from 1966, ω_{w66} to 1999, ω_{w99}.

4.6 Compression Brake

For applications in Intelligent Transportation Systems (ITS) like cruise control, driver braking assist, and autonomous highway systems, a fully modulated engine retarder would be more desirable than the existing technology that uses a fixed brake valve timing. We define the brake valve timing, v_{eb}, as the number of crank angle degrees from when the piston is at top-dead-center at the end of the compression stroke to the opening of the brake valve. The following figure, Figure 7 shows compression braking power for two different brake valve timings.

Control of the brake valve timing will allow us to continuously vary the retarding power of the compression brake mechanism. The left plot in Figure 8 shows the fixed activation of the brake valve events based on the mechanical link between the crankshaft and the camshaft. Here, the valve timing is completely determined by the engine speed. The right plot in Figure 8, on the other hand, shows a system where the valves are activated by electro-mechanical or electro-magnetic actuators. The

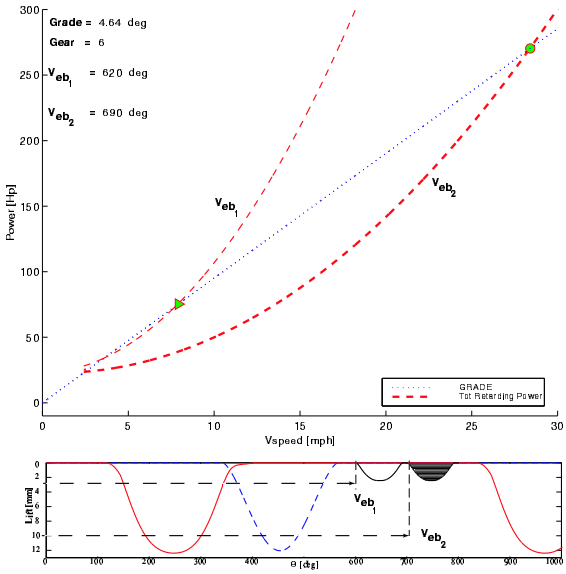

Figure 7: Variable Engine Retarder.

mechanical connections between the valve profile and the crankshaft are replaced by electronics, hence continuous variable valve timing is possible.

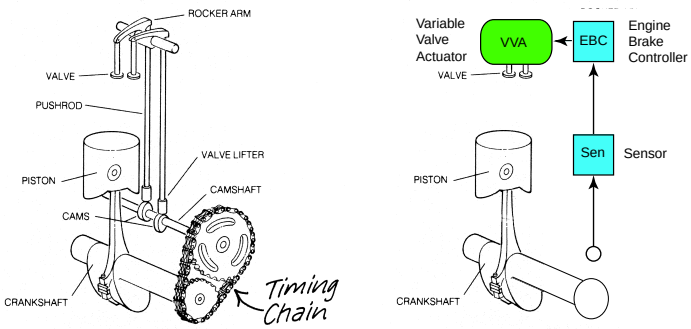

Figure 8: **Left:** Conventional valve lift system for fixed valve timing (Source: [19]). **Right:** Valve lift system that enables variable valve timing.

5 Engine Modeling

Evaluation of the dynamic system response requires an accurate yet simple model of the cylinder-to-cylinder gas exchange process and combustion. During compression, the working fluid is the air (no combustion), therefore, thermodynamic models are generally accurate. In the following sections we document the mathematical model that describes the engine operation during combustion mode (red, dashed line in Figure 3), during braking mode (black, solid line in the same figure), and during transition from one mode to the other. We also consider the engine response to crankshaft speed changes and to brake valve timing changes. Analysis of the braking effort during valve timing changes sheds light into a variable retarding mechanism that can be potentially integrated with the friction brakes. The inputs to the model are: (i) fuel flow, (ii) engine speed, and (iii) brake valve opening (fixed duration and profile). The model is capable of representing transitions from combustion to braking by cutting-off the fuel injection and initiating the brake event. The crank angle representation allow us to capture the cylinder-to-cylinder interactions and in-cylinder pressures that dictate the dynamic phenomena during the transition from combustion to braking. Based on the crank angle based model, we derive a mean-value representation of the steady-state and the dynamic characteristics of the engine braking mechanism for control design and integration with the vehicle dynamics and service brakes. Further control development will be tested in the crank angle based model.

5.1 Crank Angle Based Model

The nonlinear dynamic engine model consists of static elements (described by empirical equations), and dynamic elements (described by physically based equations). The parameters of the nonlinear static relations are determined by regression analysis of data collected from an experimental engine equipped with an engine braking mechanism. The simulation model has been implemented on a Simulink/Matlab environment using C-coded S-functions.

5.1.1 Notation

To summarize our notation, masses are defined by m, pressures, p, temperatures, T, flows, W, efficiencies, η, powers, P, volumes, V. We use the subscript c for compressor, t for turbine, i for the intake manifold, e_f, e_r, and e_c for the front, rear, and collector exhaust manifold, respectively. For cylinder j, we use cyl_j, where $j = 1 \ldots 6$. The flow from control volume x *to control volume* y is denoted by W_{xy}. We use, N_e, to denote engine speed in RPM, and ω_e, for speed in rad/sec.

5.1.2 State Equations, Plenums

The intake and exhaust manifolds and cylinders are modeled as plenums with homogeneous pressure and temperature distributions. The plenum model is based on the principles of the conservation of mass and energy, and the assumption of the ideal gas law, $pV = mRT$.

The gas properties in the intake manifold and the rear, front and collector exhaust manifolds are represented by two states: mass (m_i, and m_{ef}, m_{er}, m_e in kg), and pressure (p_i, and p_{e_f}, p_{e_r}, p_{e_c} in kPa). See Figure 9 for the schematic of the engine and definition of the plenums. The equations for the gas filling dynamics are derived on the basis of the total gas mass balances and ideal gas law:

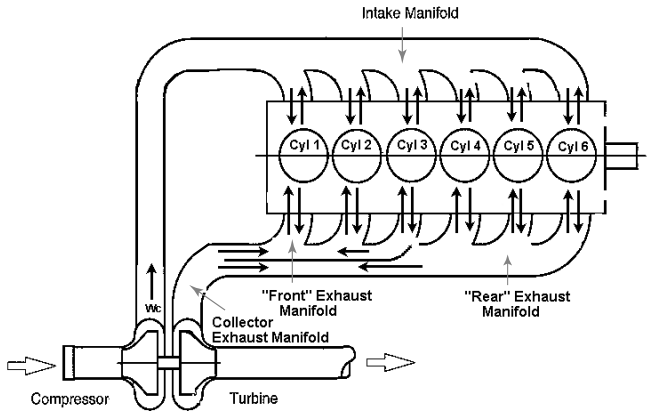

Figure 9: Schematic drawing of the engine and its control volumes.

$$\frac{dm_i}{dt} = W_c - \sum_{j=1}^{n} W_{icyl_j} + \sum_{j=1}^{n} W_{cyl_j i} \tag{11}$$

$$\frac{dp_i}{dt} = \frac{R}{V_i}\left[T_c W_c - T_i \sum_{j=1}^{n} W_{icyl_j} + T_{cyl_j} \sum_{j=1}^{n} W_{cyl_j i}\right] \tag{12}$$

where W_c and T_c are the compressor mass flow (kg/sec) and temperature (K), respectively (see Section 5.1.5). W_{icyl_j} is the mass air flow from the intake manifold into cylinder j, and $W_{cyl_j i}$ is the backflow (kg/sec)from the cylinder to the intake manifold (see Section 5.1.4). T_i and T_{cyl_j} are the intake manifold and the jth cylinder temperature (K) that is calculated based on the ideal gas law and the mass and pressure states in these control volumes.

Similarly, the state equations for the front exhaust manifold dynamics describe the rate of change of mass (m_{e_f}) and pressure (p_{e_f}) in the front exhaust manifold:

$$\frac{dm_{e_f}}{dt} = \sum_{j=1}^{3} W_{cyl_j e_f} - \sum_{j=1}^{3} W_{e_f cyl_j} - W_t \tag{13}$$

$$\frac{dp_{e_f}}{dt} = \frac{R}{V_{e_f}}\left[\sum_{j=1}^{3} T_{cyl_j} W_{cyl_j e_f} - \sum_{j=1}^{3} T_{e_f} W_{e_f cyl_j} - T_{e_f} W_{e_f e_c}\right], \tag{14}$$

where $W_{cyl_j e_f}$ is the mass air flow (kg/sec) out of cylinder j into the front exhaust manifold. This flow is calculated based on the flow through restriction equations (see Section 5.1.3) and a constant orifice equation based on geometric data. Also, W_t is the turbine mass flow (kg/sec) (see Section 5.1.5). V_{ef} is the exhaust manifold volume (m^3), and T_{ef} is the front exhaust manifold temperature (K). The state equations for

the rear exhaust manifold mirror the equations for the front one directly. The state equations for the exhaust collector manifold, on the other hand, are given by:

$$\frac{dm_{e_c}}{dt} = W_{e_f e_c} - W_{e_c e_f} + W_{e_r e_c} - W_{e_c e_r} - W_t \quad (15)$$

$$\frac{dp_{e_c}}{dt} = \frac{R}{V_{e_c}} \left[T_{e_f} W_{e_f e_c} - T_{e_c} W_{e_c e_f} + T_{e_r} W_{e_r e_c} - T_{e_c} W_{e_c e_r} - T_{e_c} W_t \right], \quad (16)$$

where W_t is the flow through the turbine (kg/sec).

The state equations for the cylinder states (mass, m_{cyl_j}, and pressure p_{cyl_j}) include the time varying cylinder volume (V_{cyl_j}) and heat transfer and release description:

$$\frac{dm_{cyl_j}}{dt} = W_{icyl_j} - W_{cyl_j i} - W_{cyl_j e} + W_{ecyl_j} \quad (17)$$

$$\frac{dp_{cyl_j}}{dt} = \frac{\gamma}{V_{cyl_j}} \left(RT_i W_{icyl_j} - RT_{cyl_j} W_{cyl_j i} - RT_{cyl_j} W_{cyl_j e} + RT_e W_{ecyl_j} - \dot{V}_{cyl_j} p_{cyl_j} \right) + \frac{\gamma - 1}{V_{cyl_j}} W_{afb_j} Q_{lhv}, \quad (18)$$

where we for simplicity have coupled e_f and e_r to one variable e. We calculate the released heat based on the apparent burned fuel rate (W_{afb}, kg/sec), and the lower heating value of light duty diesel fuel (Q_{lhv}, J/kg). In the calculation of the apparent burned fuel rate W_{afb} we have coupled the heat transfer. Thus, the integral of the apparent fuel burnt rate over a cycle is less that the averaged mass fuel injected:

$$W_{afb_j} Q_{lhv} = W_{fb_j} Q_{lhv} + Q_{ht} \quad (19)$$

$$\int_0^{\Delta T} W_{afb_j} dt < W_f \Delta T, \quad (20)$$

where Q_{ht} is the heat transfer, and W_f is the cycle (ΔT) averaged fuel flow (kg/sec). The burned fuel rate , W_{fb}, is calculated using the Wiebe approximation of the heat released during the premixed and diffusion period of the combustion (see Section 5.1.6).

The cylinder volume (V_{cyl_j}, m^3) is a functions of the crank angle (θ):

$$V_{cyl_j} = V_{cl} \left[1 + \frac{1}{2}(r_c - 1) \left(R_r + 1 - \cos\theta_j - \sqrt{R_r^2 - \sin^2\theta_j} \right) \right] \quad (21)$$

$$\theta_j = \left(\frac{N_e}{60} 360 \cdot t + 120 \cdot j \right) \bmod 720^o, \quad (22)$$

where V_{cd} is the maximum cylinder displacement volume (m^3), V_{cl} is the cylinder clearance volume (m^3), and N_e is the engine speed (RPM). The engine has six cylinders, and, therefore, a separation of 120 degrees between each cylinder, expressed by $120 \cdot j$.

5.1.3 Flow Through a Restriction

A quasi-steady model of flow through an orifice is used to derive the mass air flow through all the exhaust restrictions and the cylinder valves. The quasi-steady relation

of the air flow through a restriction is based on the assumptions of one-dimensional, steady, compressible flow of an ideal gas [17, 8].

$$W = C_d A_v \Psi(p_d, p_u, T_u), \tag{23}$$

where W is the general mass air flow (kg/sec), C_d is the discharge coefficient, A_v is the flow area function for the valve, and $C_d A_v$ is the effective flow area for the valve. The term Ψ is the standard orifice flow function that depends on the downstream pressure and temperature, p_d and T_d, and upstream pressure and temperature, p_u and T_u:

$$\Psi(p_d, p_u, T_u) = \begin{cases} \frac{p_u}{\sqrt{RT_u}} \Psi_o(\frac{p_d}{p_u}) & \text{if } p_d \leq p_u \\ 0 & \text{if } p_d > p_u, \end{cases} \tag{24}$$

with

$$\Psi_o(x) = \begin{cases} \gamma^{\frac{1}{2}} \left(\frac{2}{\gamma+1}\right)^{\frac{\gamma+1}{2(\gamma-1)}} & \text{if } x \leq c_r \\ x^{\frac{1}{\gamma}} \sqrt{\frac{2\gamma}{\gamma-1}(1 - x^{\frac{\gamma-1}{\gamma}})} & \text{if } x > c_r, \end{cases} \tag{25}$$

where $c_r = \left(\frac{2}{\gamma+1}\right)^{\frac{\gamma}{\gamma-1}}$ is the critical pressure ratio across the orifice.

5.1.4 Valve Flow

The mass air flow from the intake manifold into cylinder j, W_{icyl_j}, can be calculated using previous Equations 23-25:

$$W_{icyl_j} = f_{iv}\left(l_{iv}(\theta)\right) \cdot \Psi(p_{cyl_j}, p_1, T_1). \tag{26}$$

The effective flow area though the intake valve, $f_{iv} = C_d A_{iv}$, is calculated using crank angle data of the intake valve lift ($l_{iv}(\theta)$). Both maps are given by the engine manufacturer.

Similarly, the flow through the exhaust valve is given by:

$$W_{cyl_j e} = f_{ev}\left(l_{ev}(\theta)\right) \cdot \Psi(p_e, p_{cyl_j}, T_{cyl_j}), \tag{27}$$

where the exhaust valve map $f_{ev} = C_d A_{ev}$ is a function of the exhaust valve lift map, l_{ev}, and is provided by engine manufacturers.

The brake valve is, technically speaking, the same as the exhaust valve. The only difference is the valve lift profile. This means, that the flow through the brake valve is given by Equation 27, where $l_{ev}(\theta)$ is replaced by $l_{bv}(\theta)$. Again, this valve lift is provided by engine manufacturers.

5.1.5 Turbocharger Dynamics

The turbocharger state equation consists of the rate of change of the turbocharger speed, N_{tc}, based on the conservation of energy on the turbocharger shaft:

$$\frac{dN_{tc}}{dt} = \frac{P_t - P_c}{I_{tc} N_{tc}}, \tag{28}$$

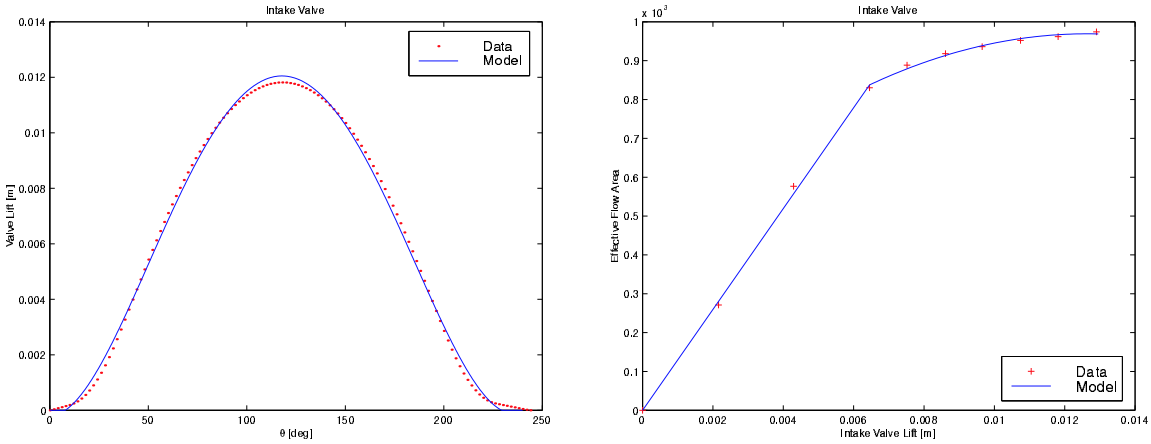

Figure 10: **Left:** Intake valve lift versus crank angle. **Right:** Intake valve effective flow area vs. valve lift

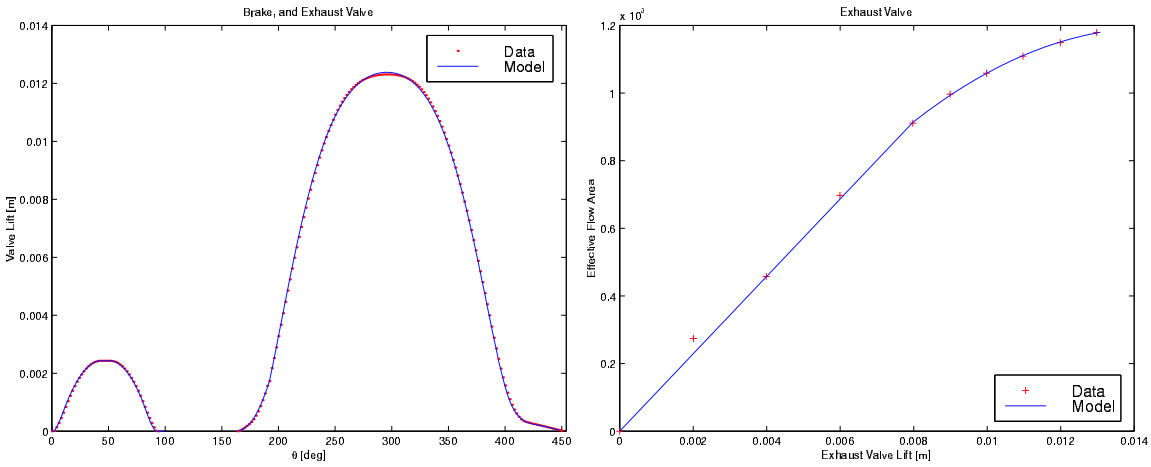

Figure 11: **Left:** Exhaust and brake valve lift versus crank angle. **Right:** The effective flow area for both the exhaust valve and the brake valve vs valve lift

where P_t is the turbine power, the P_c is the compressor power, and I_{tc} is the mass polar moment of inertia of the turbocharger. P_t and P_c are calculated based on an ideal adiabatic process, and steady-state data provided by the turbocharger manufacturer.

In particular, turbine maps, f_{t_w} and f_{t_η}, are used to determine the mass air flow, W_t and the efficiency, η_t. Both turbine maps are functions of the turbocharger speed, N_{tc}, and the pressure ratio, r_t, across the turbine.

$$
\begin{aligned}
P_t &= W_t c_p \eta_t T_2 \left(1 - \frac{1}{r_t}^{\left(\frac{\gamma-1}{\gamma}\right)}\right) && (29)\\
W_t &= f_{t_w}\left(N_{tc}, r_t\right) && (30)\\
\eta_t &= f_{t_\eta}\left(N_{tc}, r_t\right) && (31)\\
r_t &= \frac{p_2}{p_0},
\end{aligned}
$$

where p_0 is the ambient pressure, and c_p is the specific heat capacity for constant pressure.

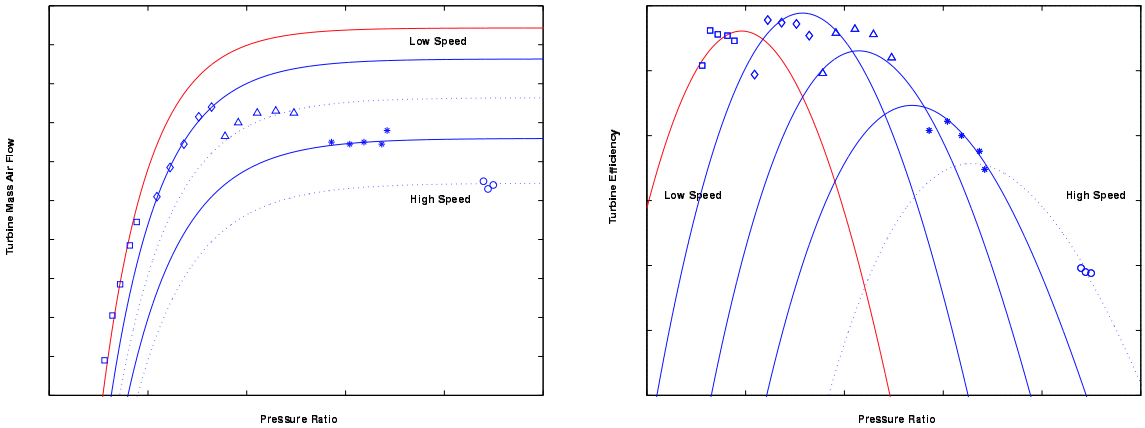

Figure 12: **Left:** Map for turbine mass flow, W_c. Right: Map for turbine efficiency, η_t.

Similarly, using data from the compressor maps we obtain the compressor characteristics given below:

$$
\begin{aligned}
P_c &= W_c T_0 \frac{c_p}{\eta_c}\left(r_c^{\left(\frac{\gamma-1}{\gamma}\right)} - 1\right) && (32)\\
W_c &= f_{c_w}\left(N_{tc}, r_c\right) && (33)\\
\eta_c &= f_{c_\eta}\left(N_{tc}, r_c\right) && (34)\\
r_c &= \frac{p_1}{p_0}
\end{aligned}
$$

where f_{c_w} is the compressor map for mass flow, and f_{c_η} is the map for the compressor efficiency, η_c. Both of these maps are functions of the turbocharger speed, N_{tc}, and the pressure ratio, r_c, across the compressor.

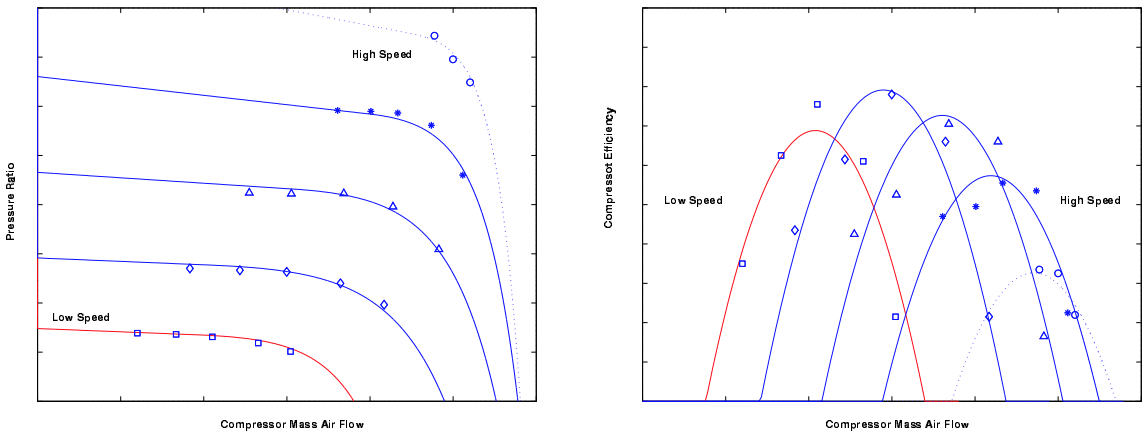

Figure 13: **Left:** Map for compressor mass air flow, W_c. **Right:** Map for compressor efficiency, η_t.

5.1.6 Apparent Fuel Burn Rate

The apparent burn fuel rate was identified based on cylinder pressure data and modification of Equation 18 for zero flow into and out of the cylinder:

$$W_{afb} = \frac{1}{Q_{lhv}(\gamma - 1)} \left(\gamma p_{cyl} \frac{dV_{cyl}}{dt} + V_{cyl} \frac{dp_{cyl}}{dt} \right) \tag{35}$$

We assume above that heat capacities are constant and couple the heat transfer to the calculation of an effective or apparent fuel burn rate. We stress here that the apparent fuel burn rate we calculate above is less than the actual fuel burn rate. This is because we, for simplicity, assume zero heat losses.

The apparent fuel burn rate curves for ten speed and load points were used to develop a crank angle functional approximation. Two Wiebe basis functions have been combined to capture the premixed and the diffusion burning:

$$W_{afb} = max \left(W^d_{afb}, W^p_{afb} \right) \tag{36}$$

$$W^d_{afb} = C_d k_{d2} \left(k_{d1} + 1 \right) \theta_d^{k_{d1}} \exp \left(-k_{d2} \theta_d^{(k_{d1}+1)} \right) \tag{37}$$

$$W^p_{afb} = C_p k_{p1} k_{p2} \left(1 - \theta_p^{k_{p1}} \right)^{(k_{p2}-1)} \theta_p^{(k_{p1}+1)} \tag{38}$$

The variables $\theta_d = \frac{\theta - \theta_{soc}}{\Delta\theta_d}$ and $\theta_p = \frac{\theta - \theta_{soc}}{\Delta\theta_p}$ are defined over the diffused combustion duration, $\Delta\theta_d$, and the premixed combustion duration, $\Delta\theta_p$, respectively. To simplify the data fitting, we assumed that both premixed and diffused-based combustion start at the same time, i.e., at start of combustion, θ_{soc}. Using the max function in the combination of the two curves in Equation 36 resolves the two distinct starts for premixed and diffused-based combustion, as shown in Figure 14.

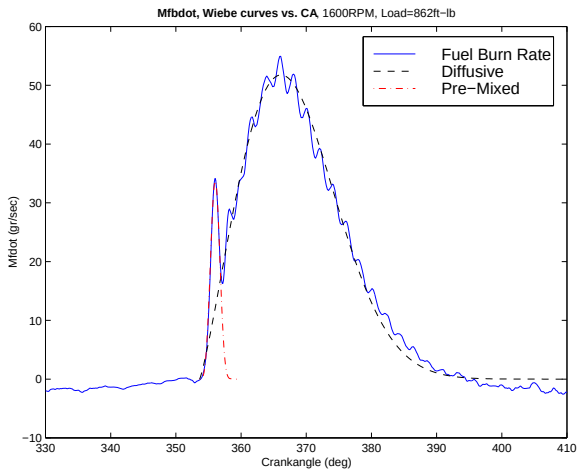

Figure 14: Combustion analysis and apparent fuel burn rate.

The start of combustion is computed based on the start of injection θ_{soi} and the ignition delay $\Delta\theta_o$:

$$\theta_{soc} = \theta_{soi} + \Delta\theta_o \tag{39}$$

The six coefficients C's and k's, the two combustion mode durations, $\Delta\theta$'s, and the ignition delay $\Delta\theta_o$ have been identified and regressed on fuel injected and engine speed

using the ten available data points. A good compromise between data over-fitting and small prediction errors is achieved with polynomials of second order in fuel flow and first order in engine speed for all variables.

We also regressed the start of injection θ_{soi} based on fuel input and engine speed. Although, this does not give us the flexibility to use the injection timing as another model input, it allows us to maintain the simple combustion analysis in our model. The predicting ability of the developed model in fuel injection timing changes can be examined in future work.

5.1.7 Shaft Torque

The torque produced at the crankshaft during combustion, or, transmitted from the crankshaft during braking, TQ_{cyl_j}, is calculated based on the individual cylinder pressure and piston motion using the idealized slider-crank mechanism [21]:

$$TQ_{cyl_j} = p_{cyl_j} \frac{\pi B^2}{4} r \sin(\theta_j) \left[1.0 + \frac{r}{R} \frac{\cos(\theta_j)}{\sqrt{1.0 - \left(\frac{r}{R}\sin(\theta_j)\right)^2}} \right] \tag{40}$$

The shaft torque is calculated by the summation of the individual cylinder torque. The average torque from the piston to the shaft during combustion is positive and the average torque from the shaft to the piston during braking is negative. Defining positive and negative torque allow us to seamlessly integrate the combustion mode and the braking mode and use the fuel flow and brake valve timing, $[v_f, v_{eb}]$ as one actuator (see Section 5.1.8, Figure 21).

5.1.8 Engine Simulation Results

The engine model has been implemented in Matlab/Simulink using S-functions. It has 23 states with significantly different rates of convergence (stiff system), and multiple discontinuous functions that have been implemented with *if-else* statements. The stiffness and discontinuity are handled satisfactory with the *ode23s* integration algorithm (one-step solver based on a modified Rosenbrock formula) within Matlab. Simulation of the engine model during a transition from combustion to braking is shown in Figure 15. The simulation is performed at constant engine speed, $N_e = 1600$ RPM, as the first subplot on the left indicates. The last plot in the right column shows the fuel flow command. One can clearly see the fuel cutoff at the fifth cycle. At that point the software is implemented to run with zero fuel (motoring) for one cycle before it opens the brake valve at $v_{eb} = 685^o$. This brake valve command is shown in the last plot in the left column of Figure 15. The model has been implemented with one cycle delay between the combustion and the braking mode to avoid extrapolation errors. It is shown that if we do not introduce this delay in the transition process the turbine efficiency drops below 0.2 which is outside the model region of validity. The delay can be viewed by observing the trace of cylinder pressure in the third plot of the left column.

The traces of intake and exhaust manifold pressure, as well as the turbocharger speed, demonstrate the importance of the turbocharger dynamics in predicting the transient torque response. The instantaneous torque response is shown in the fourth plot in the right column. One can see that the time necessary to transition from the

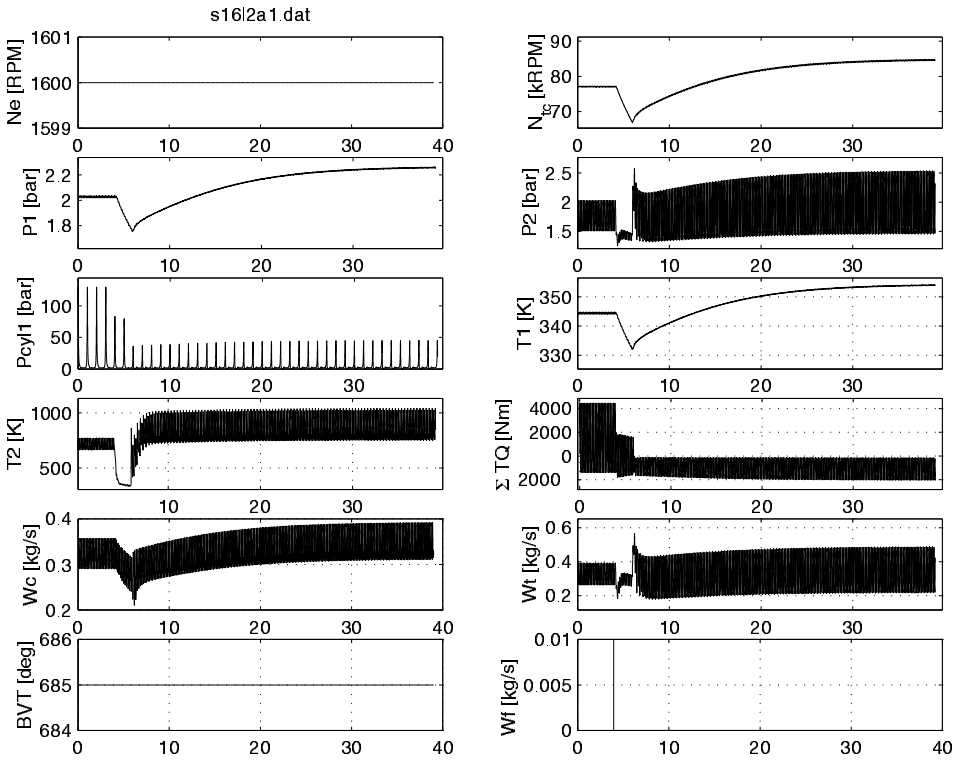

Figure 15: Simulation response during transition from combustion to braking.

steady-state combustion mode to steady-state braking mode is approximately equal to **ten cycles**. It is also evident that a first order lag will not be adequate to capture the mean-value behavior. Detailed analysis and signal processing of the simulation data follow in the next section. However, the above rough estimate of settling time indicates that the actuator dynamics will dominate the engine dynamics. Currently, the conventional devices have a fixed delay of approximately 0.6 sec, which is necessary to pump-up the system's hydraulic pressure sufficiently to open the brake valve against the high cylinder pressure. For comparison, we state here that conventional friction brakes that are pneumatically actuated, have a typically 0.3 sec delay, and a pneumatic pressure transient of 0.5 sec.

The plots clearly show that that interactions between the compression brake and the turbocharger dynamics are important to the retarding performance of the engine. Recent work by Hu et al. [9] emphasize the importance of such interactions. Dynamic coupling between the compression effort and the turbocharger power determines the engine response during the transient operation of switching back to the conventional power generation mode.

5.2 Model Order Reduction

In this section we derive a series of local linear models of low order that capture the mean-value dynamic behavior of the engine. It is easy to see from Figure 15 that the dominant dynamics are in the order of cycles and not in the order of crank angles. As a matter of fact, we would like to average all the quasi-period crank angle based dynamics. Analytically this can be done using singular perturbations, but such a rigorous treatment is not currently available. Developing such analytical techniques is an active research topic. Meanwhile, we can process simulation data using numerical techniques, such as signal processing and system identification tools. We perform here all the necessary steps to obtain a low, 3rd. order model from the original 23rd. order that captures the dominant transient characterization.

To develop an input-output model with brake valve timing, v_{eb}, engine speed, N_e, and fuel flow, v_f as inputs, and torque, TQ, as output, we run the crank angle based model with small step changes in v_{eb}, N_e, and v_f around a nominal point. The results are shown in Figure 16. The third plot in Figure 16 shows the event-averaged

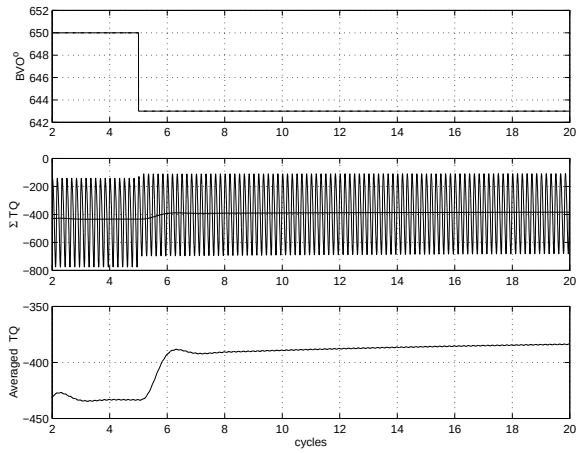

Figure 16: Simulation input/output data and lowpass output.

torque response. We obtain the cycle-averaged response by processing the crank angle torque output with a third order Butterworth filter with a cutoff frequency of $\frac{1}{720}$ Hz. Furthermore, we use the output error, **oe**, model in the identification toolbox of Matlab, to estimate a low order model that can approximate the averaged output torque response, ΔTQ, based on step changes in brake valve timing, Δv_{eb}, engine speed, ΔN_e, or fuel flow Δv_f.

5.2.1 Braking Mode

Figure 17 shows a first and a third order approximation for how a seven degree step change up and down in brake valve timing around $v_{eb} = 685^o$ affects the output torque,ΔTQ. The engine speed is kept constant at $N_e = 1500$ RPM. The third order approximation is the best one. In fact, it is hard to distinguish it from the averaged torque trace. The third order transfer function is given by:

$$\frac{\Delta TQ}{\Delta v_{eb}} = \frac{0.039s^2 - 9.631s - 12.82}{0.001s^3 + 0.0501s^2 + 1.7558s + 1.6417} \tag{41}$$

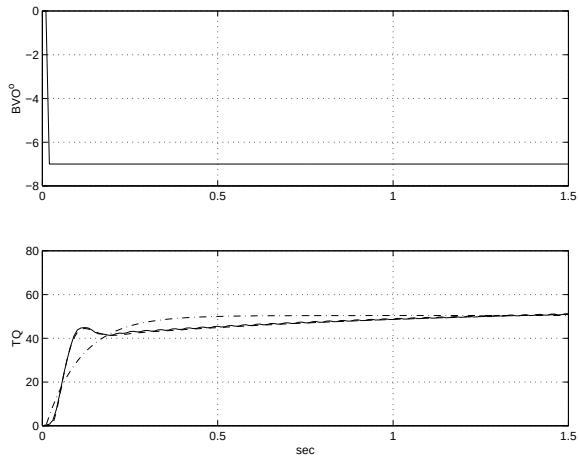

Figure 17: Prediction error estimate of an output-error model using 3rd order (dashed), and 1st order (dashed-dotted).

By repeating the procedure with step changes in v_{eb} and N_e for several operational points, we obtain a family of linear third order models. Note here that a step up and a step down from the nominal point is required for the complete characterization of the nonlinear crank angle based model. The left plot in Figure 18 shows the Bode frequency response for the linear model for seven degrees step changes in brake valve timing up and down around $v_{eb} = 685^o$ for $N_e = 750$, 1500, and 2100 RPM. The right plot in Figure 18, on the other hand, shows the frequency response for ten percent step changes in $N_e = 750$, 1500, and 2100 RPM, for fixed $v_{eb} = 650^o$. The following

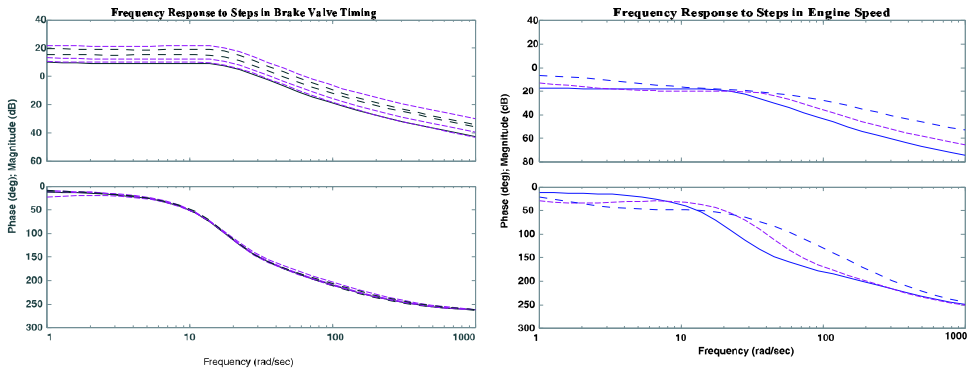

Figure 18: **Left:** Frequency response for steps in v_{eb}. **Right:** Frequency response for steps in N_e.

third order transfer function, describes the reduced order, linear dynamics for a 150 RPM step change up and down in engine speed around $N_e = 1500$ RPM, when the brake valve timing is kept fixed at $v_{eb} = 650^o$:

$$\frac{\Delta TQ}{\Delta N_e} = \frac{-0.517s^2 + 152.6s + 479}{s^3 + 51.33s^2 + 1656s + 1611} \tag{42}$$

5.2.2 Switching Mode

From the frequency plots in Figure 19, we note that the switching mode is governed by faster dynamics than the braking mode. The left plot in Figure 19 shows the frequency response for switching from combustion mode, with fuel flow, $v_f = 10$ g/sec, to braking mode with brake valve timing, $v_{eb} = 650^o$. The speed is kept constant at $N_e = 1600$ RPM. The right plot in Figure 19, on the other hand, shows the exact opposite process, that is switching from braking to combustion. It is very interesting to note that switching *from* braking to combustion mode (left plot in Figure 19) is a slower process than switching from combustion *to* braking mode (right plot). This is, however, experimentally observed by Cummins, 1966 and Hu, 1992.

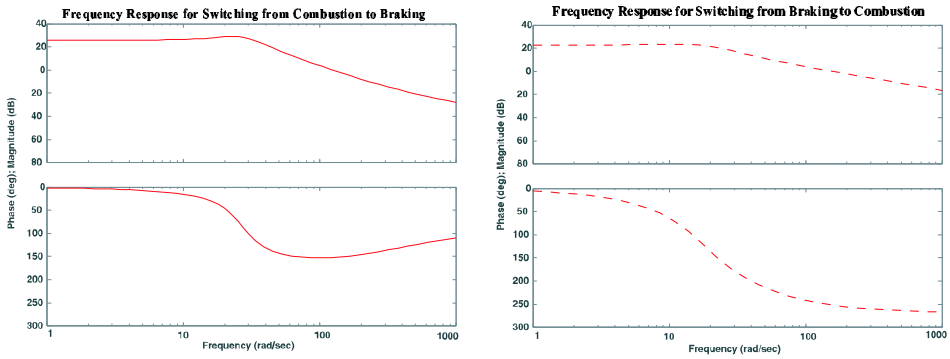

Figure 19: **Left:** Frequency response for switching from combustion *to* braking. **Right:** Frequency response for switching *from* braking to combustion.

The following equation, Equation 43, gives the second order transfer function that describes the linear model for switching from combustion mode *to* braking mode.

$$\frac{\Delta TQ}{\Delta v_f} = \frac{38s + 14091}{s^2 + 19.74s + 738.1} \tag{43}$$

5.2.3 Combustion Mode

The following figure, Figure 20, shows the frequency response for a ten percent step change up and down in fuel at $N_e = 1600$ RPM. The combustion mode is governed by slower dynamics than the braking mode. In [12], they report that the maximum turbocharger speed is lower during compression braking than it is during operation with combustion. On the other hand, the turbine accelerates faster during compression braking than during increase in fuel level. Another intricate phenomenon arises during operation in high altitude [12]. Specifically, the turbine speed decays at high altitude instead of increasing, as occurs during normal engine operation. The coupling between the turbocharger and the engine dynamics is further augmented with transmission and driveline interactions and is reported in [16].

5.3 Static Engine Map

By combining the fuel flow, v_f, and the brake valve timing, v_{eb}, into one actuator, we produce a static map of generated and absorbed engine brake power shown in Figure 21. Positive values indicating v_f, and negative values indicating v_{eb}.

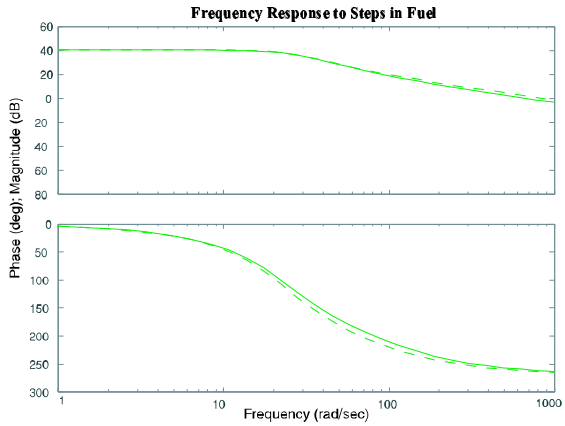

Figure 20: Frequency response for step changes in fuel at $N_e = 1600$ RPM.

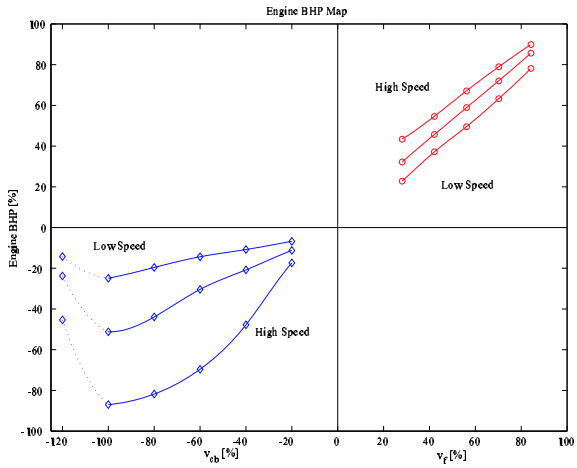

Figure 21: Generated and absorbed engine brake power plotted versus a unified engine actuator, that combines the fuel flow, v_f, and the brake valve timing, v_{eb}, into one input signal.

An interesting observation is that the rate of change for the brake torque changes sign for high valve timings (dotted line in Figure 21). However, the torque sign reversal is eliminated by imposing one fixed saturation level on the upper limit of, v_{eb}, on the expense of potentially of loosing the ability to reach maximum brake torque at each speed.

By using a standard linear regression method on the data when the fixed saturation level is imposed, the brake torque can be expressed in the following way:

$$TQ_{eb} = \alpha_0 + \alpha_1 v_{eb} + \alpha_2 v_{eb}^2 + \alpha_3 \omega_e + \alpha_4 v_{eb} \omega_e \tag{44}$$

The brake torque is quadratic in brake valve timing, v_{eb}, and linear in engine speed, ω_e, if v_{eb} is kept constant.

6 Model Validation

To validate the developed model, we compare model outputs with selected measurements from an experimental engine at an engine-dynamometer facility.

6.1 Mean Value Model Validation

In Figure 22 we compare mean-value engine and brake shaft power, for steady-state engine conditions. The upper part of the plot shows the engine running in combustion mode, for nine different speed and fueling levels. Overall, the predicted values from our model (+) indicate an error less than about thirteen per cent from the measured values (o). However, if we neglect the lowest fueling level, the error is approximately six percent.

In the lower part of the plot, we compare modeled and measured compression brake power for nominal brake valve timing, v_{eb}^{nom}, and for six different speeds. The deviation between measured and modeled peak power for high speed ($N_e \geq 1600$ RPM), is due to hardware limitations of the actuator on the experimental engine. Depending

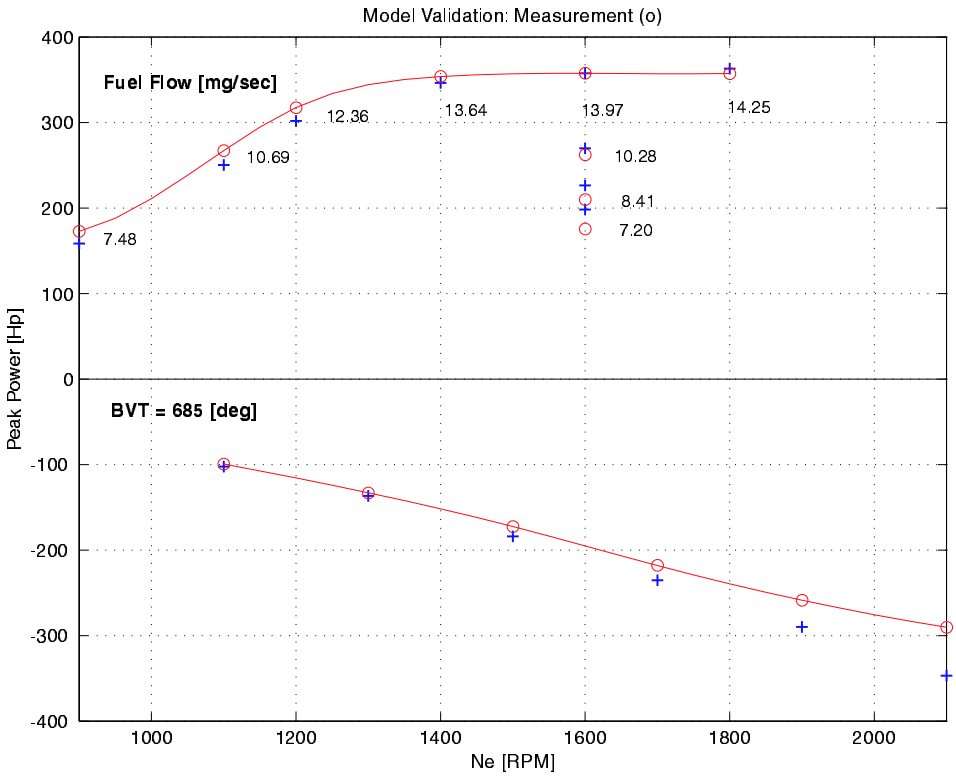

Figure 22: Comparison of predicted and measured mean-value shaft power.

on the operating speed, the maximum error between modeled and measured values is less than seven percent for low speed, and less than 20 percent for high speed ($N_e \geq 1600$ RPM).

6.2 Steady State Model Validation

Another way to validate our modeling work is to compare modeled and measured steady-state cylinder pressure in the crank angle domain. The four plots in Figure 23 show modeled and measured cylinder pressure for the engine operating in both combustion and braking mode, for different speed and loads.

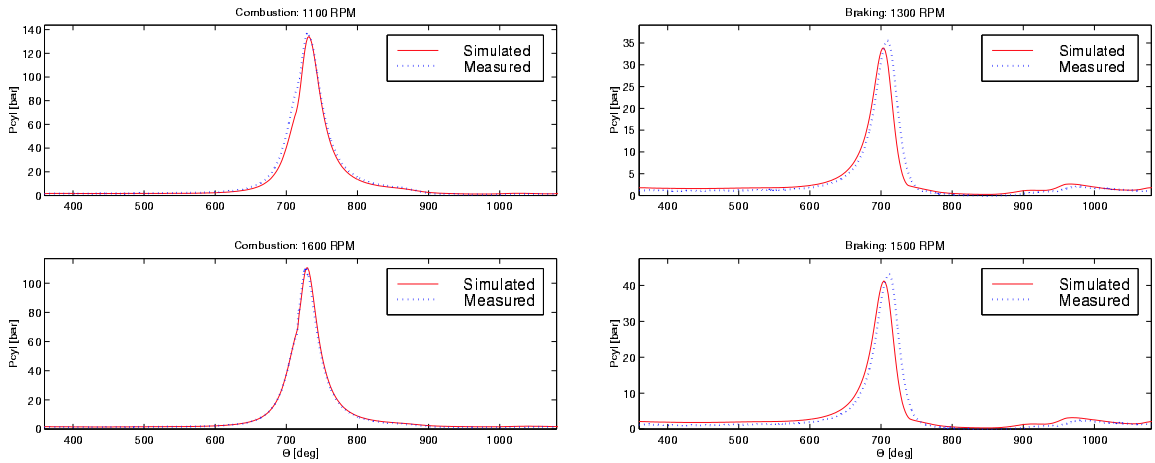

Figure 23: **Left:** Comparison of modeled and measured cylinder pressure for different speed and load during combustion mode. **Right:** Comparison of modeled and measured cylinder pressure for different speed and load during braking mode.

The lower left plot in Figure 23 shows *qualitatively* an almost perfect match between modeled and measured cylinder pressure. However, to *quantify* how well the developed model match the experimental engine, we calculate mean and standard deviation for the residual vector, $E = P_{mes} - P_{mod}$, for each simulation case. The following table lists the key statistical measures for the combustion mode:

Combustion:	$N_e = 1100$	$N_e = 1600$	Total
Mean	1.16	- 0.44	0.36
Standard deviation	2.63	0.98	2.14

The mean value of the residual vector is zero for a perfect match, while the mean value is - 0.4 bar for the data shown in the lower left plot in Figure 23. Based on the standard deviation, we predict that 95 percent of the data is within $\pm$ 2 bar from the mean. The reason why this particular case match the experimental data so well is that this case was used to calibrate the model during the modeling phase.

The upper left plot indicates a very good match for an operating point not used for calibration. The mean value of the residual vector is 1.2 bar, and 95 percent of the data for modeled cylinder pressure are predicted to be within $\pm$ 5.3 bar from the mean.

The comparison for the braking mode, shown in the two plots in the right column of Figure 23, is not quite as impressive as the one for the combustion mode. One reason for this is that, although we use the same nominal brake valve timing as the test engineers did when they collected the data, it is impossible to measure when the valve opening really occurred. A small deviation from the nominal value will affect the cylinder pressure. Again, to quantify the match, the following table of the key statistical measures for the braking mode is used:

Braking:	$N_e = 1300$	$N_e = 1500$	Total
Mean	- 0.19	- 0.33	- 0.26
Standard deviation	2.39	3.11	2.77

Overall, the mean value for the residual vector is around - 0.3, and 95 percent of the braking data are predicted to be within $\pm$ 5.5 bar from the mean.

7 Speed Control Problem Formulation

The following set of equations describes our system:

$$\dot{x} = f(x,u,w) \quad (45)$$
$$y = x \quad (46)$$

where x denotes the states in the system, $u = [u_{eb}, u_{sb}]^T$, and w denotes the grade, β. Equation 45 is the state space representation of Equation 7. Our control objectives can be summarized in the following way:

(A) Regulation problem: $\omega_e \rightarrow \omega^{des}$ as $t \rightarrow \infty$, where ω^{des} is constant.

(B) Tracking problem: $\omega_e \rightarrow \omega^{des}(t)$

(C) Disturbance rejection: achieve (A) and (B) during unknown torque disturbance introduced by rapid changes in grade, β.

(D) Achieve (A), (B), and (C) taking into account significant parameter variations in mass, M, gear, r_g, and rolling resistance, μ. To be able to this, we have to use robust and adaptive control techniques.

8 Analysis of the Longitudinal Vehicle Model

Using the results from the compression brake modeling section, Section 5, we obtain the full nonlinear longitudinal vehicle dynamics. In this section, we first linearize the model around a nominal point, before we use frequency domain and time domain response analysis to quantify the open-loop sensitivity to parameter variation.

8.1 Linearization of Longitudinal Vehicle Dynamics

The longitudinal vehicle model is given in Equation 47:

$$J_T \frac{d\omega_e}{dt} = TQ_{eb}(v_{eb},\omega_e) + r_g\left(F_\beta(\beta) - F_{sb}(v_{sb}) - F_a(\beta) - F_r(\beta)\right) \quad (47)$$

Linearization of Equation 47 around a nominal point, indicated by $|_0$, leads to the following expression:

$$\begin{aligned} J_T \frac{d}{dt}(\Delta\omega_e) = {} & \frac{\partial TQ_{eb}}{\partial v_{eb}}\Big|_0 \Delta v_{eb} + \frac{\partial TQ_{eb}}{\partial v_{eb}}\Big|_0 \Delta\omega_e - r_g M g \cos(\beta_0)\Delta\beta \\ & - r_g \frac{\partial F_{sb}}{\partial v_{sb}}\Big|_0 \Delta v_{sb} - \rho C_d A_v r_g^3 \omega_{e_0}\Delta\omega_e - \mu M g \sin(\beta_0)\Delta\beta \end{aligned} \quad (48)$$

Laplace transformation of Equation 48 results in following linear model for the vehicle dynamics:

$$\begin{aligned} J_T s\Delta\omega_e(s) = {} & G_{eb_v}(s)\Delta v_{eb}(s) + G_{eb_\omega}(s)\Delta\omega_e(s) + G_\beta(s)\Delta\beta(s) \\ & + G_{sb_v}(s)\Delta v_{sb}(s) + G_a(s)\Delta\omega_e(s) + G_r(s)\Delta\beta(s) \end{aligned} \quad (49)$$

Grouping of terms, and closing the internal feedback loop that exists for the compression brake, the following expression describes the vehicle dynamics:

$$\omega_e(s) = \left(\frac{G_{eb_v}(s)}{J_T s - G_{eb_\omega}(s) + \rho C_d A_v r_g^3 \omega_{e_0}} \right) \Delta v_{eb}(s) \quad (50)$$

$$- \left(\frac{r_g G_{sb_v}(s)}{J_T s - G_{eb_\omega}(s) + \rho C_d A_v r_g^3 \omega_{e_0}} \right) \Delta v_{sb}(s) \quad (51)$$

$$- \left(\frac{r_g M g \left(\cos(\beta_0) + \mu \sin(\beta_0)\right)}{J_T s - G_{eb_\omega}(s) + \rho C_d A_v r_g^3 \omega_{e_0}} \right) \Delta \beta(s) \quad (52)$$

where $G_{eb_v}(s)$ is given by the transfer function in Equation 41, and $G_{eb_\omega}(s)$ is given by Equation 42. $G_{sb_v}(s) = r_g F_{sb}(s)$, where $F_{sb}(s)$ is given by the Laplace transformation of the linearized Equation 2.

8.2 Frequency Domain Analysis of Linearized Vehicle Dynamics

Figure 24 shows the frequency response of the transfer functions from each of the three inputs: $v_{eb}(s)$, $v_{sb}(s)$, and $\beta(s)$, to the speed output, $\omega_e(s)$. Included in the

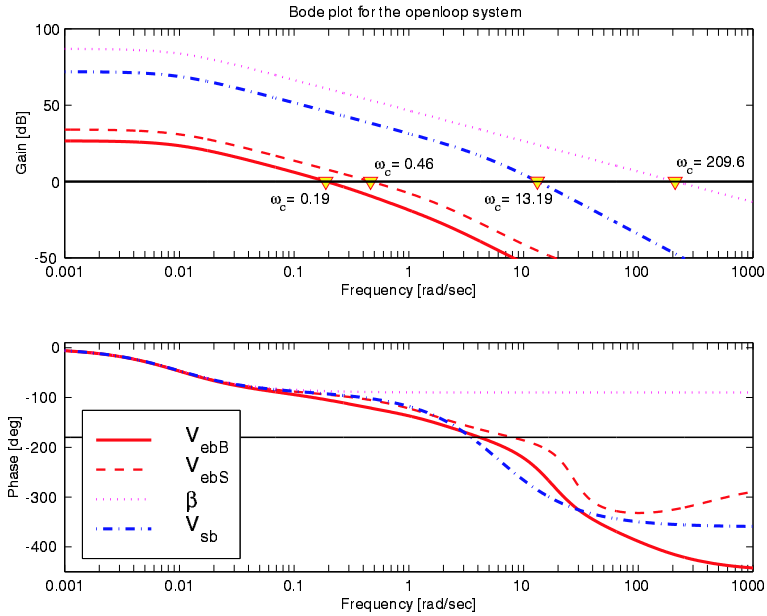

Figure 24: Bode plot for the open-loop system.

plot in Figure 24 is also the dynamics of the engine retarder when we switch from combustion to braking mode. Although "lowpassed" through the vehicle rotational dynamics, it is clear that the these two modes are governed by different dynamics (see also discussion in Sections 5.2.1 and 5.2.2).

8.3 Sensitivity Analysis

In this subsection, we use time and frequency domain analysis to investigate how sensitive the linear vehicle dynamics are to parameter variations.

The first two columns in Figure 25 show the frequency response for the transfer function, G_{eb}, as defined in Equation 50, for variations in gear ration, r_g (column one), and vehicle mass, M (column two). The two plots in the third column, on the other hand, show the corresponding step responses for the same parameter variations. For variations in the gear ratio, r_g, given in the first column in Figure 25, the DC

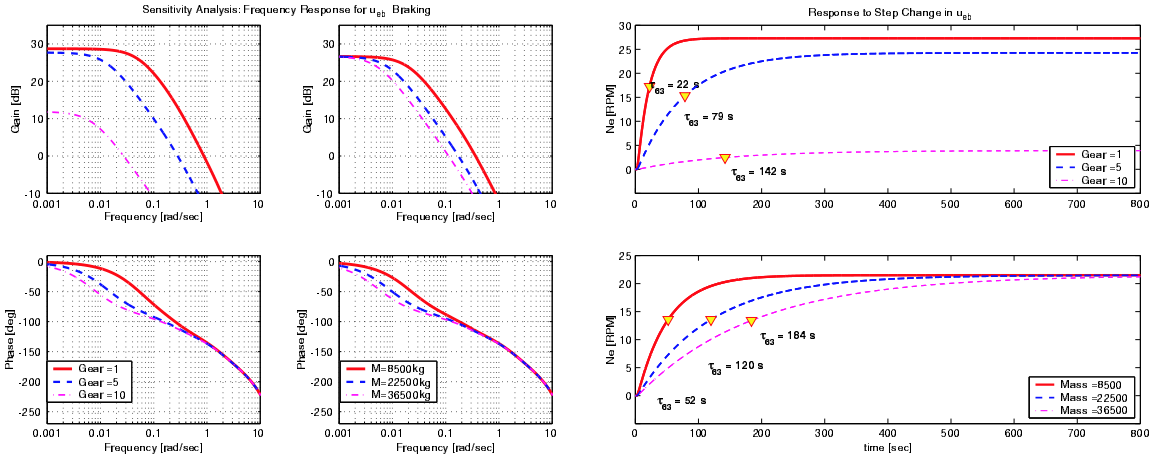

Figure 25: Sensitivity of G_{eb} to parameter variations in gear ratio, r_g, and vehicle mass, M.

gain takes values between $12 - 29$ dB. Converting the numbers from dB to amplitude ratio, reveals a difference in amplification of about seven. A commanded brake valve timing, v_{eb}, has seven time more control authority in gear number one than in gear number ten.

If we define the frequency for zero dB as the cross-over frequency, ω_c, then we see that ω_c varies from about 0.02 rad/sec for gear number one, to about 0.9 rad/sec for gear number ten. From the step response plot (upper right corner), we see that the time constant, τ_{63} varies from about 22 sec for gear number one, to about 142 sec for gear number ten. This is a significant variation of about 640 percent.

A CHV is a vehicle system that can have various configurations. Due to this, the total mass for a CHV can vary with more than 400 percent, from being a system of tractor alone, to being a system of tractor pulling a fully loaded trailer. Column two in Figure 25, shows how the frequency response look like for that kind of variation in vehicle mass. First of all, the DC gain is not affected by variations in vehicle mass, M. This is also seen in the step response plot, in the lower right corner of Figure 25. Here, we see that the time constant, τ_{63} varies between about 52 sec for tractor alone, to about 184 sec for the combination of tractor and a fully loaded trailer. The variation in the time constant is about 350 percent.

The first two columns in Figure 26, on the other hand, show the frequency response for the transfer function, G_β, as defined in Equation 52, for variations in gear ration, r_g (column one), and vehicle mass, M (column two). The two plots in the third column show the corresponding step responses for the same parameter variations. In column one in Figure 26, we show the step response for variations in gear ratio, and the most noticeable feature is that gear number one produces the lowest amplification but has the highest cross-over frequency, compared to other gear ratios. The reason for this is that r_g is in the numerator of G_β (Equation 52). The gear ratio, r_g, is 0.012

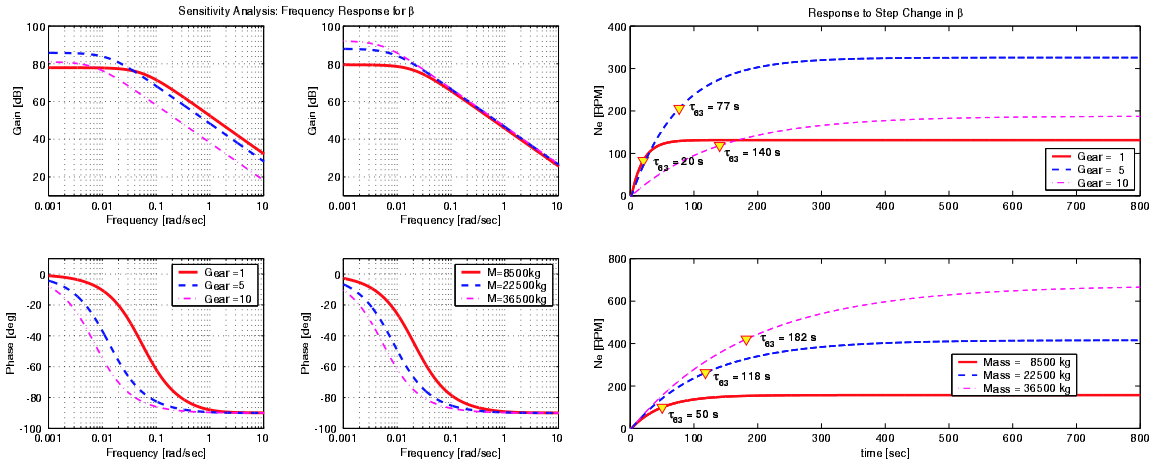

Figure 26: Sensitivity of G_β to parameter variations in gear ratio, r_g, and vehicle mass, M.

for gear number one, and 0.12 for gear number ten, hence, by shifting to a higher gear ratio, the amplification increases. The denominator of G_β, on the other hand, produces the highest gain and the highest cross-over frequency for gear number one. The overall result is that the magnitude of the frequency response for gear number one is pulled down. The corresponding step response is shown in the upper right corner of Figure 26. The plot clearly shows that gear number one has lower amplification, but faster time constant than gear number five and ten.

Variations in vehicle mass, as seen in column number of Figure 26, result in spread of about 15 dB in the DC gain. The step response, in the lower right corner, show that the variation in time constants is about 300 percent.

8.4 High Priority Controller Design

In this section, we develop a coordinated braking controller using classical control methods. Our control objectives in this phase of the project are to regulate the engine speed, ω_e, and to reject torque disturbances introduced by changes in the grade, β. The controller design is based on the linear vehicle dynamics given in Equation 50, and Ziegler and Nichols' classical approach to tune a PID controller:

$$u(t) \quad = \quad k_p \left(e(t) + \frac{1}{\tau_I} \int_0^t e(\tau) d\tau + \tau_D \frac{de(t)}{dt} \right)$$

The Z-N PID-Controller settings, based on finding the ultimate gain and period, K_u and P_u, respectively, were empirically developed to provide a 1/4 decay ratio, which in most cases is regarded to be too oscillatory. We have, therefore, decided to use a modified "no overshoot version of the PID settings, as given in [20]. K_u and $P_u = \frac{2\pi}{\omega_{180}}$ can be easily identified using Figure 27. The definitions of L, S, and T, are as follows:

$$\begin{array}{lll} L & = G_{eb} G_c & \text{loop transfer function} \\ S & = (I + G_{eb} G_c)^{-1} \qquad = (I + L)^{-1}, & \text{sensitivity function} \\ T & = (I + G_{eb} G_c)^{-1} G_{eb} G_c \quad = (I + L)^{-1} L, & \text{complementary sensitivity function} \end{array}$$

where G_c denotes the controller transfer function, and G_{eb} denotes the transfer function defined in Equation 50.

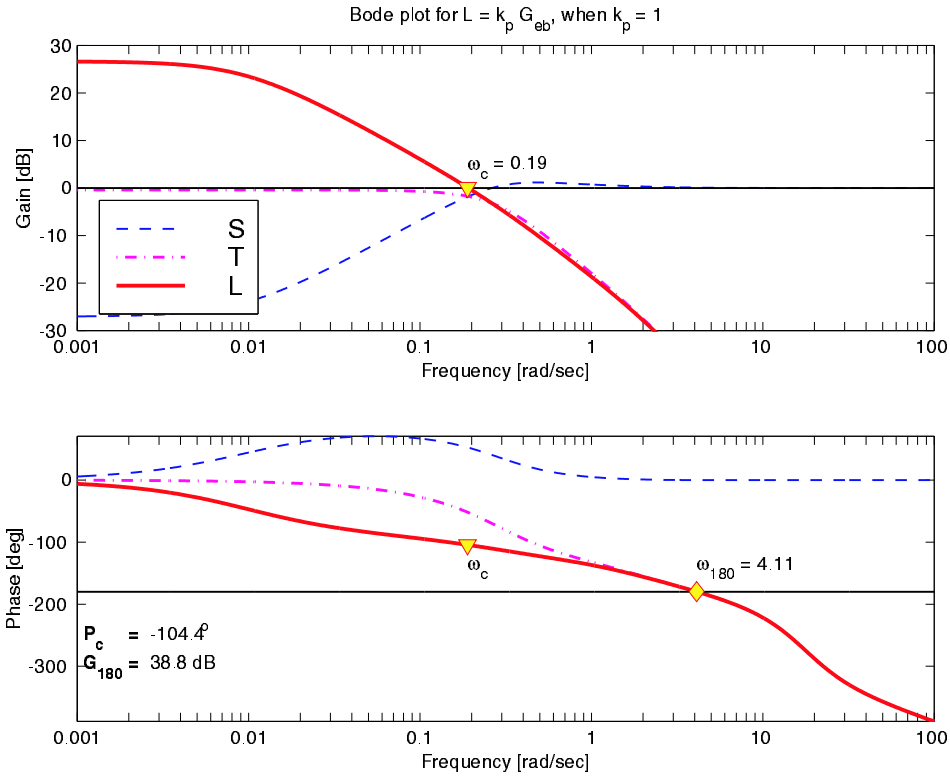

Figure 27: Bode plot for $L = k_p\, G_{eb}$ for $k_p = 1$.

Here, $K_u = 88$, while $\omega_{180} = 4.1$ rad/sec $\Rightarrow P_u = 1.5$ sec. Based on the "no overshoot" version of the Z-N method, we derive the following parameters:

$$\begin{aligned} k_p &= 0.2\ K_u \Rightarrow & k_p &= 17.6 \\ \tau_I &= P_u/2 \Rightarrow & \tau_I &= 0.8\ sec \\ \tau_D &= P_u/3 \Rightarrow & \tau_D &= 0.5\ sec \end{aligned}$$

For the implementation of the PID controller, we use a filtered version of the derivative action, since the ideal derivative term is unrealizable. The following equation, Equation 53, shows the transfer function for the PID controller we implemented.

$$G_c(s) = \frac{u_{eb}(s)}{e(s)} = k_p \left(\frac{\tau_I s + 1}{\tau_I s}\right)\left(\frac{\tau_D s + 1}{\alpha \tau_D s + 1}\right) \tag{53}$$

The α in Equation 53 is a small number, typically between 0.05 and 0.2. Here, $\alpha = 0.2$.

There are no design specifications for longitudinal performance of CHVs. To be able to quantify stability and robustness properties of our controlled system, we adapted the commonly accepted upper bounds on S and T, as defined in [23]: $M_S = \| S \|_\infty$ should be less than about 6 dB and $M_T = \| T \|_\infty$ should be less than about 2 dB. In terms of gain and phase margins, $M_S < 6$ dB implies the common design rule, $GM > 6$ dB and $PM > 30^o$. Values larger than 12 dB on either S or T indicate poor performance as well as poor robustness.

Figure 28 shows the frequency response for L, S, and T, as defined in Equation 53, with the controller settings as given in Eg. 53. The peak value of $\| S \|$ is $M_S = 7.2$

dB, and the peak value of $\| T \|$ is $M_T = 7.6$ dB which are high according to our design specifications.

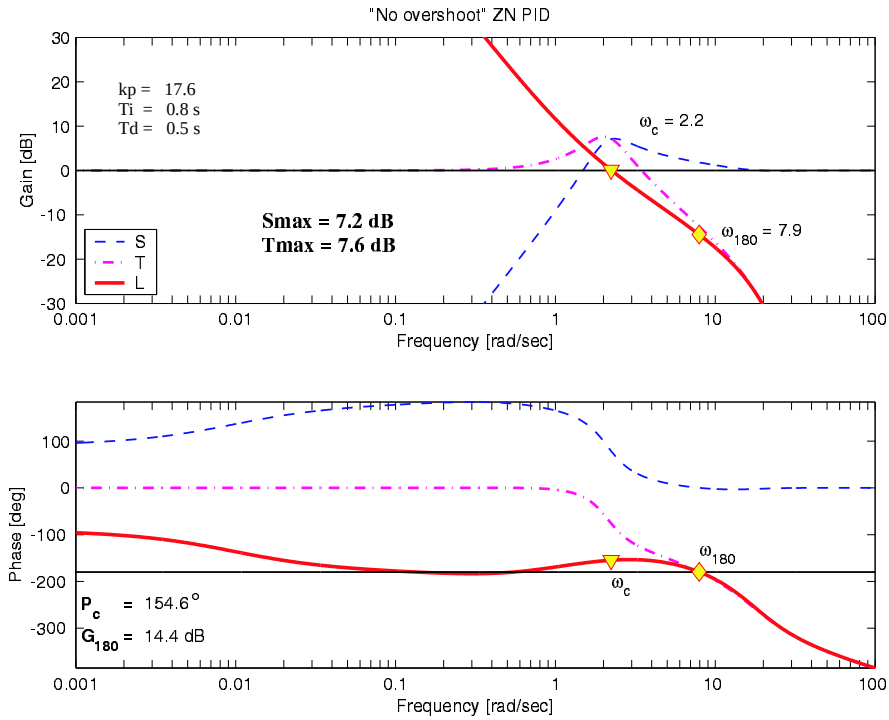

Figure 28: Frequency response for control system using the "no overshoot" version of the Z-N method.

Due to the previous controller's high M_S and M_T values, we retune the controller. We decide to leave out the derivative action, since that term can cause noise problem in the real application. Our conclusion based on this preliminary analysis and control design, is that even for the linear nominal plant, we need to increase the controller complexity beyond a simple PI or PID controller. We will pursue this lead in future work, but we continue here with a PI controller that achieves a reasonable performance for all the three modes of engine operation. We choose $k_p = 5$ and $\tau_I = 5$ sec, and plot the frequency response in Figure 29 Figure 29 shows that the peak value of $\| S \|$ and $\| T \|$ are $M_S = 5.1$ dB, and $M_T = 4.8$ dB, respectively. M_T is still higher than our design specification. However, this is the best we can do when we in Section 8.5 want to simulate five critical longitudinal maneuvers using a single PI-controller setting.

Coordination of the compression brake with the service brakes is achieved based on a P-controller on the service brakes:

$$u_{sb}(t) = k_s \left(v_{eb} - sat(v_{eb}) \right) \tag{54}$$

The P-controller is activated when the compression brake saturates, hence it assigns low priority to the service brakes, reducing the use of them unless it is necessary. The block diagram of the controller scheme is shown in Figure 30 .

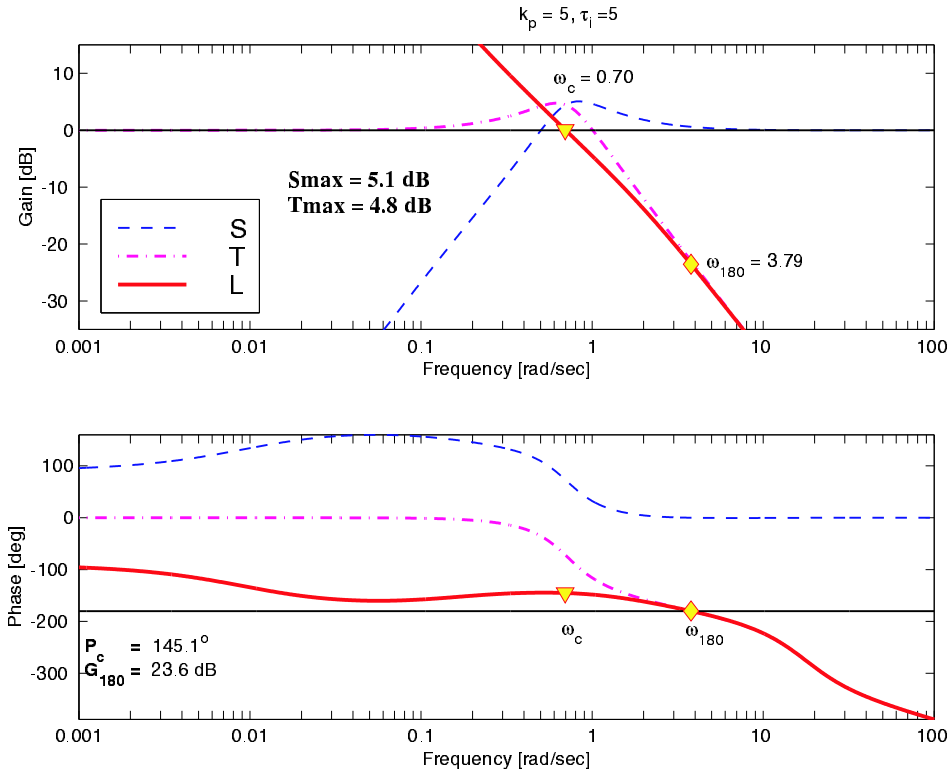

Figure 29: Frequency response for control system using a compromised controller setting.

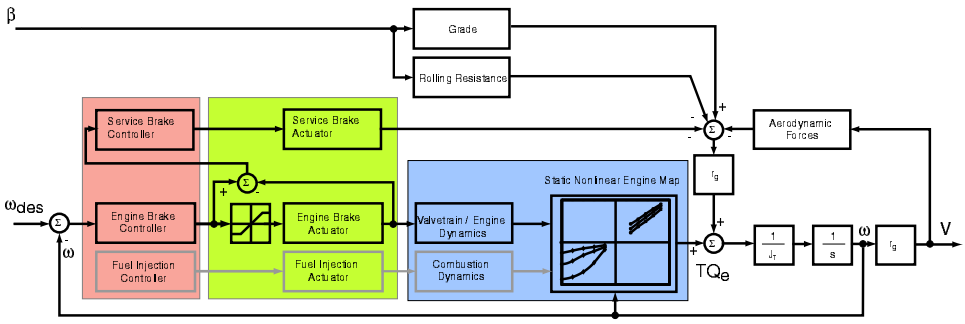

Figure 30: Block diagram for a coordinated braking controller.

8.5 Simulation Results

Simulation results of the designed longitudinal closed-loop system are included in this section. The simulations show the closed-loop performance of the nonlinear simplified vehicle model coupled with the high priority PI-controller. We identify five critical longitudinal maneuvers for which engine braking is instrumental. These maneuvers or driving scenarios are typical for CHVs and, thus, important for the assessment of our work. The first driving scenario tests the closed-loop performance during a small step input change of the desired vehicle speed. The second scenario demonstrates the disturbance rejection capability of the closed-loop system. The two first scenarios are within the linear operating region of the controller, so the service brakes are not activated. In the last three scenarios, large retarding demands are required.

Specifically, in scenario three, a large step change in grade while in braking mode causes saturation of the compression brake. In scenario four, a small step change in grade while in combustion mode causes the activation of the compression brake and switching from combustion to braking. And finally, a large step change in grade while in combustion mode, triggers and saturates the compression brake and activates the service brakes, in scenario five.

In the following Figures 31-35, the right plot contains important engine and vehicle variables plotted on the same time axis, with the desired step changes in vehicle speed or road grade. The left column in each of the same figures, shows the phase plot of the retarding power versus vehicle speed. The phase plot demonstrates the importance of a non equilibrium analysis of the system behavior.

Driving Scenario 1

The driving scenario shown in Figure 31, illustrates a CHV in braking mode with a constant descending speed of 16.6 mph at a constant road grade of 4^o. At t =2 sec, a unit step change in desired speed is required. The phase plot shows the speed-power trajectory between the two equilibrium points. The time plots to the right show the compression brake effort and the braking torque on the engine shaft. The last time subplot shows a small undershoot in the vehicle speed before settling to the new equilibrium value after 14 seconds.

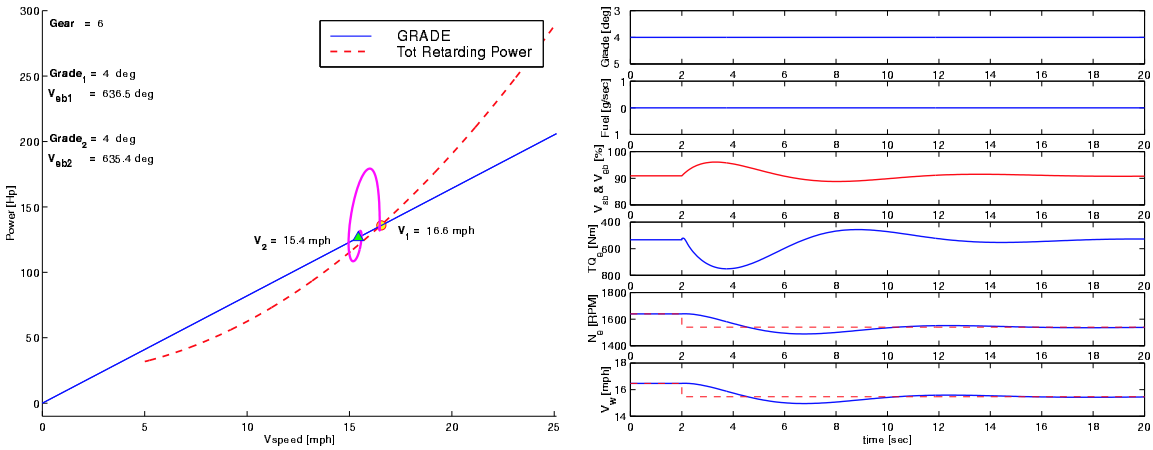

Figure 31: Step change in speed, closed-loop control of v_{eb}.

Driving Scenario 2:

Figure 32 shows the simulation results of a CHV in braking mode, and on a 5^o grade. At t = 2 sec, a step change in grade from 5^o to 7^o is introduced, and again speed regulation and disturbance rejection are the objectives. As seen in the last time subplot in Figure 32, the speed increases slightly before returning to its initial value. The torque disturbance due to the step change in grade is effectively rejected by the closed-loop control scheme, and a stable and safe descending speed is achieved using the compression brake alone.

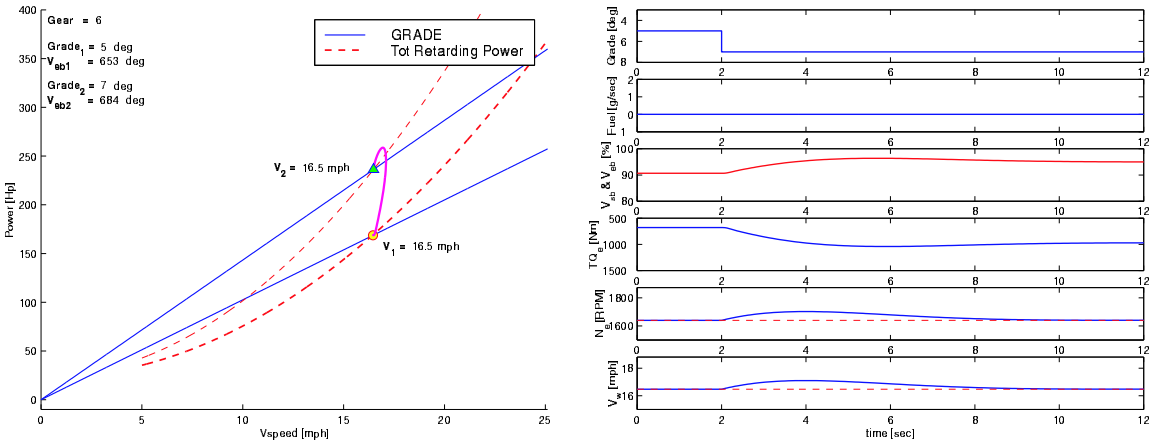

Figure 32: The system rejects torque disturbance introduced by a small step change in grade.

Driving Scenario 3

In the third simulation, shown in Figure 33, the CHV is once again in braking mode, and on a road with a descending grade of 5^o. This time, however, the step change in grade at $t = 2$ sec is from 5^o to 9^o, too large for the compression brake to handle alone. Upon saturation of the compression brake, the service brakes are activate, and the vehicle speed is regulated to its desired value.

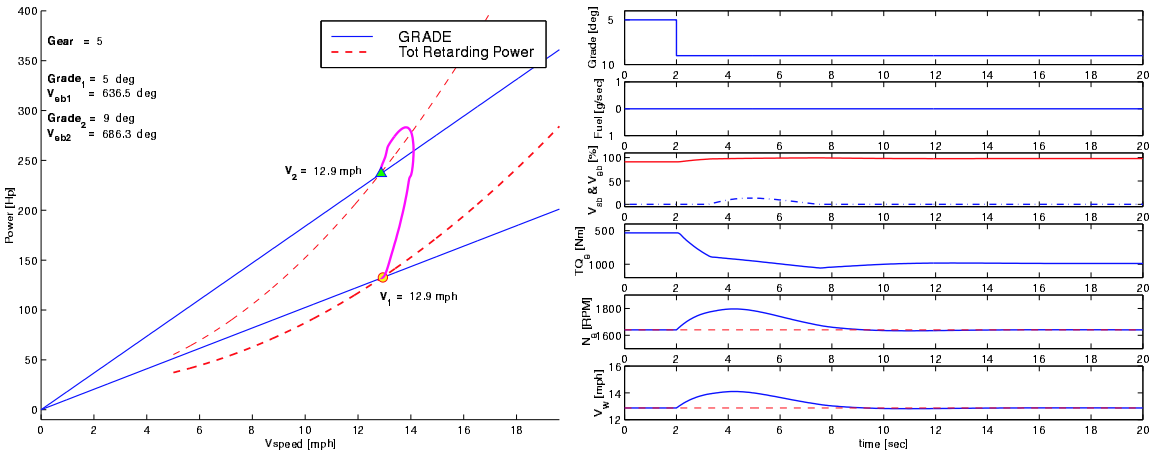

Figure 33: Large step change in grade requires the use of service brakes.

Driving Scenario 4

Figure 34 shows the resulting trajectories for a transition from combustion to braking. Initially, the CHV is cruising on a flat terrain at a constant speed. At $t = 2$ sec, the CHV enters a descending grade of 3^o, and at that time we see in the time subplots 2 and 3 in Figure 34, that the controller cuts off the fuel and activates the compression brake. Speed regulation is achieved without using the service brakes.

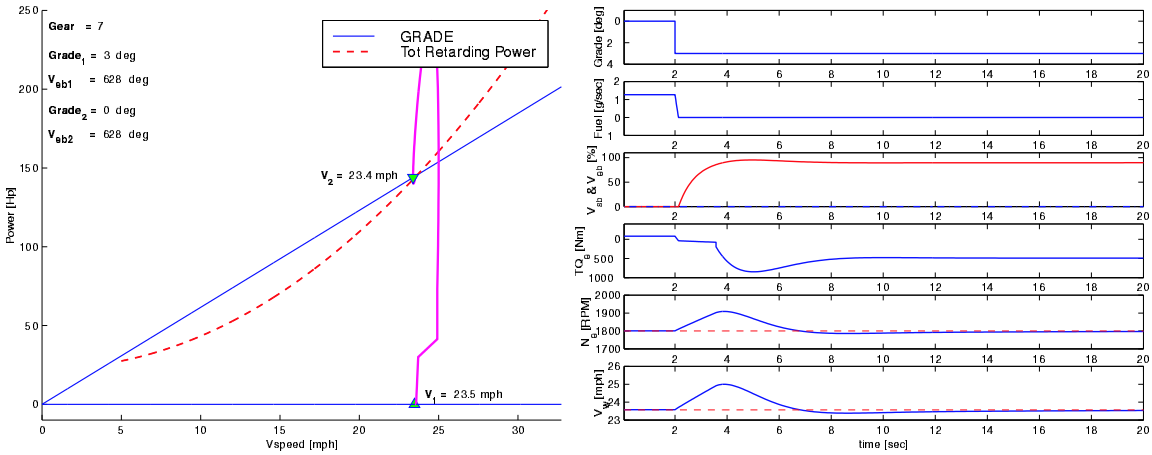

Figure 34: Switching from combustion to braking.

Driving Scenario 5

In the fifth and most demanding driving scenario, shown in Figure 35, the CHV is once again cruising on a flat terrain with fuel flow, $v_f = 1.2$ g/sec. At $t = 2$ sec, the vehicle encounters a large descending grade of 6^o, and time subplot 2 shows the fuel cut. Time subplot 3, on the other hand, shows first the activation, and then the saturation of the compression brake. Immediately following the saturation of the compression brake, the service brakes are activated through the high priority controller. By coordinating theses two actuators once again, the vehicle descending speed is regulated using a PI-controller on the compression brake, and a P controller on the service brakes.

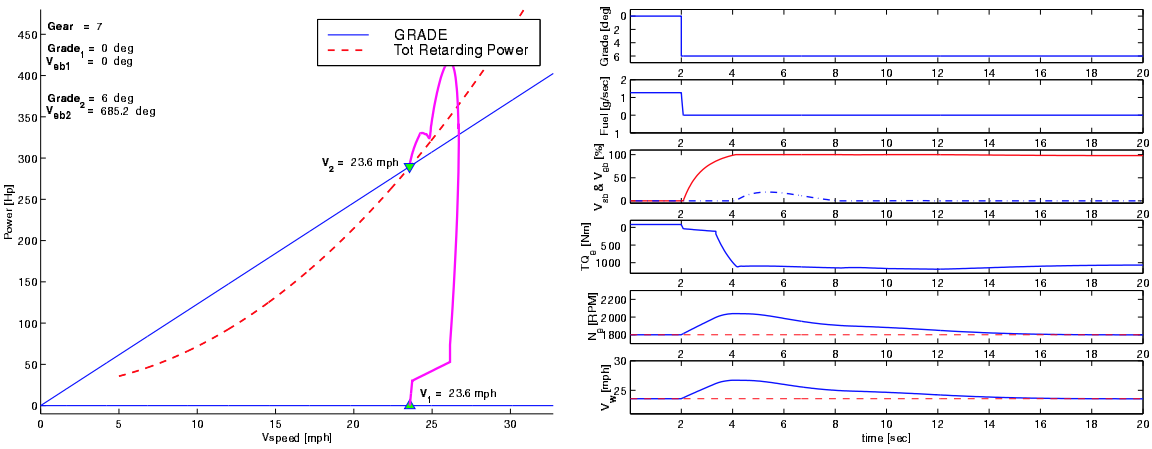

Figure 35: Switching from combustion to braking. This time the grade change is large and forces the system to apply service brakes.

8.6 Remarks on the Simulation Results

To assess the improvements we achieve using the CBC controller scheme, we simulate the same five driving scenarios described in Section 8.5, with the compression brake disabled. That is, we use PI-control on the service brakes only (SBO).

To quantify the improvements we achieve using the CBC controller scheme, we define the following performance index:

$$I = \int_0^{t_{set}} v_{sb}(\tau)^2 d\tau, \tag{55}$$

where the settling time, t_{set}, is defined as the time required for the service brake actuator signal, v_{sb}, to reach and remain inside a band whose width is equal to $\pm$ 5 % of the new steady state value [20].

The following Figures 36- 40, show the same five driving scenarios shown in Figure 31- 35 for both the CBC and the SBO controller scheme. In addition, the performance index defined in Equation 55, and the corresponding settling time, t_{set}, are shown

Driving Scenario 1

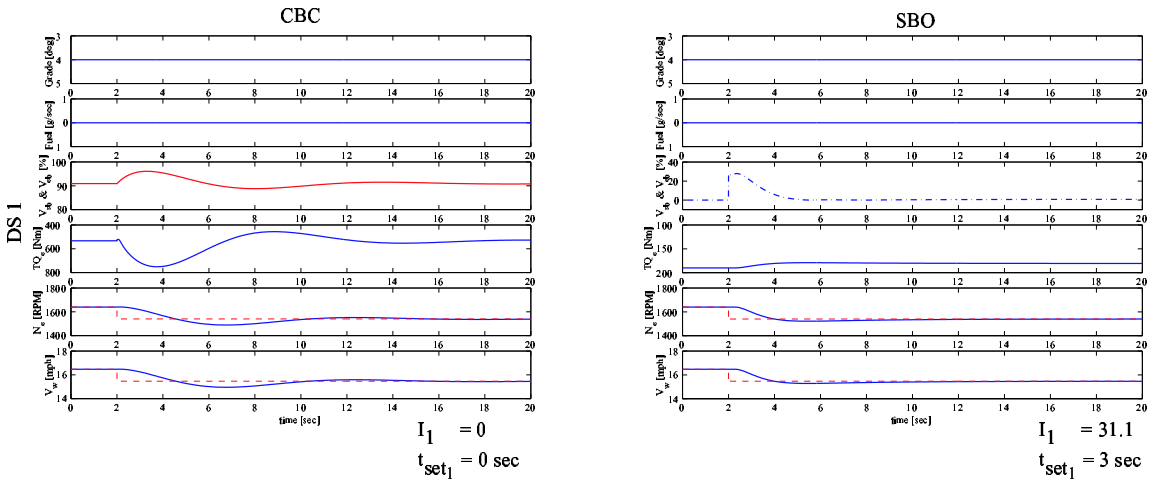

Figure 36: Step change in speed, closed-loop control of v_{eb}.

Driving Scenario 2

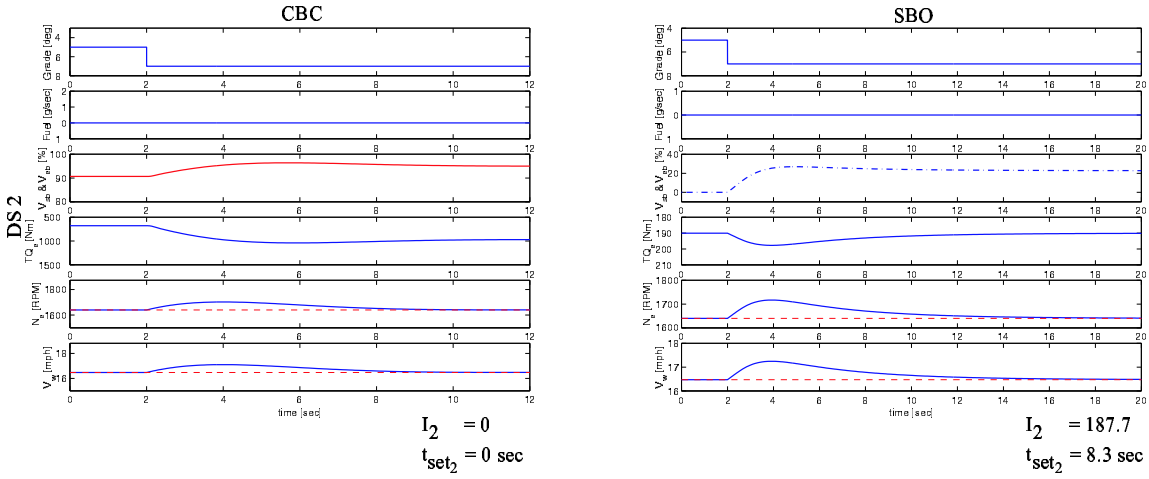

Figure 37: The system rejects torque disturbance introduced by a small step change in grade.

Driving Scenario 3

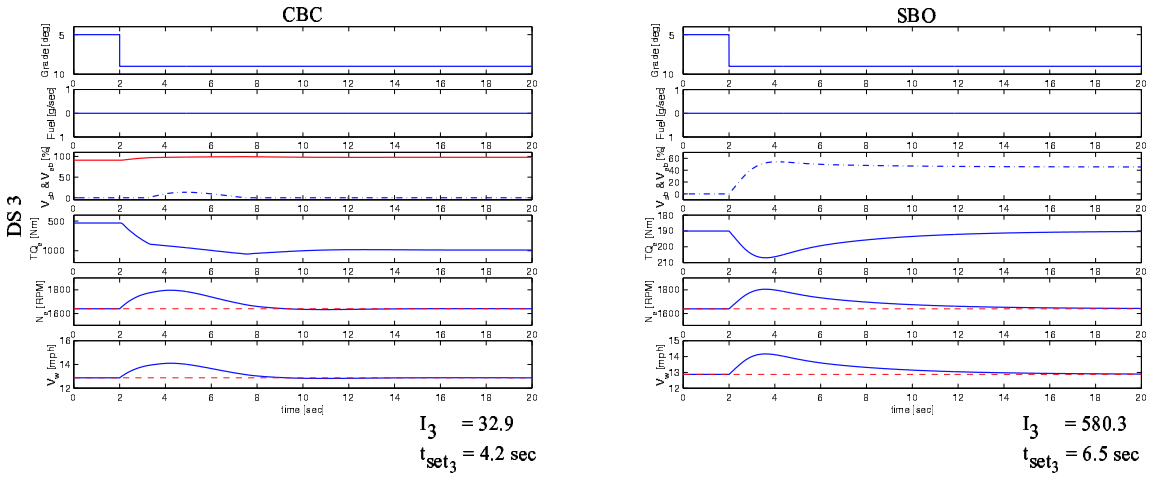

Figure 38: Large step change in grade requires the use of service brakes.

Driving Scenario 4

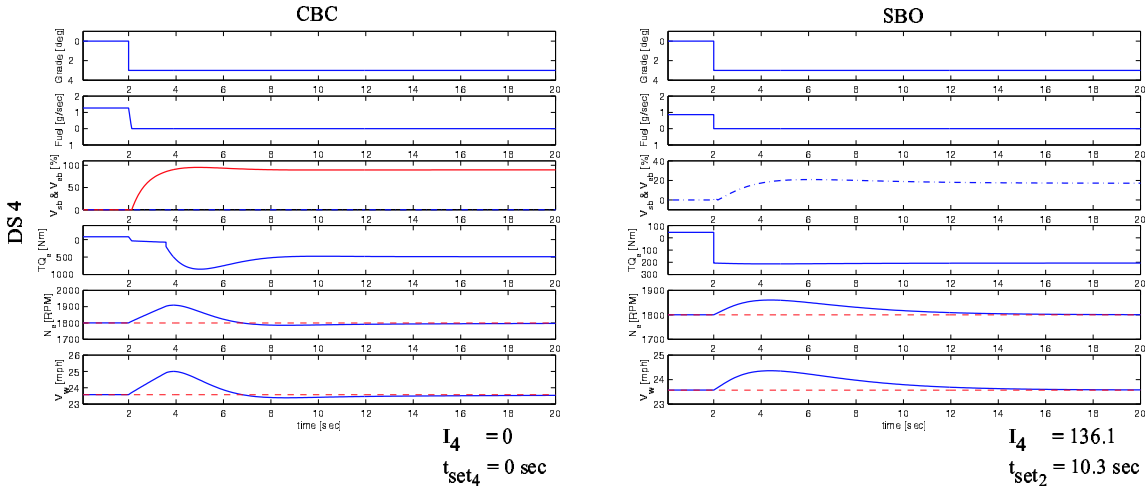

Figure 39: Switching from combustion to braking.

Driving Scenario 5

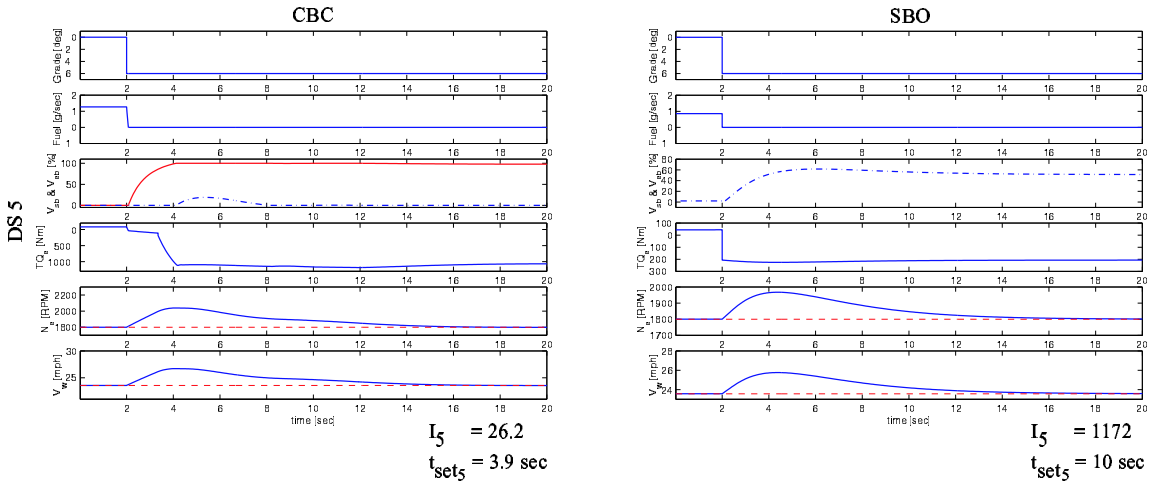

Figure 40: Switching from combustion to braking. This time the grade change is large and forces the system to apply service brakes.

In the most challenging driving scenarios, DS 3 and DS 5, service brakes are used in both the CBC and the SBO controller schemes. The ratio between SBO and CBC is approximately 17.5 for DS 3, and 45 for DS 5. This means that using a coordinated braking controller scheme in critical longitudinal maneuvers, reduces the use of service brakes by a factor of 45.

If we, in addition to comparing performance indices, compare settling times, t_{set}, for the same two driving scenarios, we see that t_{set} is reduced from about 6.5 to about 4.2 seconds for DS 3, and from about 10 to 4 seconds for DS 5. DS 5 is the most

critical longitudinal maneuver, so a decrease in the settling time by a factor of 2 is substantial when it comes to wear and tear on the friction pads in the service brakes.

9 Concluding Remarks

The key issues, research accomplishments, and directions for future work are summarized as follows:

1) Model Development

Derivation of a novel control-oriented engine model able to represent transition between combustion and braking mode, and the dynamical interactions between engine and CHV longitudinal subsystems. The key issues are:

- Integration of different time scales such as crank angle dynamics (100 μsec), gas dynamics (20 msec), and vehicle dynamics (10 sec) in a nonlinear, multivariable dynamical model.
- Model order reduction for control analysis and design. This technique of signal processing and input-output identification of step input responses, using crank angle simulation data, has application to a large class of problems in the engine control field.
- Validation of the developed models using measurements obtained from an engine-dynamometer facility.

2) Sensitivity and Control Analysis

Analysis of the dynamics shed light into the critical transient phase that quasi-steady equilibrium analysis typically conceals.

- The general, but controversial belief that the turbocharger dynamics, thus, engine acceleration, is faster during braking than during combustion mode is substantiated. This explains the high occurrence of vehicle runaways (engine acceleration above safe limits).
- Analysis of the detrimental consequences of the actuator delay and saturation levels for the stability of a CHV. Even if a stable equilibrium for descending speed exists for a given grade, vehicle mass, rolling resistance, and large actuator delays can lead to maximum engine speed ("runaway").
- Characterization of the relative control authority for the redundant retarding actuators, and their relative importance in critical braking maneuvers. Nowadays, the control allocation is primarily resolved by predictive actions of trained drivers.
- CHVs operate under considerable changes in vehicle parameters, such as gear selection, vehicle mass, aerodynamic drag, rolling resistance, etc. Some of these parameters are unknown and unmeasured, and introduce large uncertainties in the longitudinal control system.

3) Control Design (in progress)

Automation and integration of the compression brake with the service brakes is considered to be a critical task in CHV operations due to the potential increase in mobile capacity and safety. In this report, we employ classical control techniques for the design of a low order controller, that coordinates compression and service brakes, for speed regulation and disturbance rejection.

- Controller gains are tuned to maintain nominal performance and robust stability during operations in braking and transition modes.
- Anti-windup scheme is designed to account for saturation and authority allocation for the two redundant retarding actuators.

Our objective is to alleviate the robust performance limitation associated with actuator delays and model uncertainties due to large parameter variations. Few of the main obstacles in autonomous heavy vehicle following have been removed by using aggressive prediction algorithms, [26, 29]. The prediction algorithms, however, assume accurate knowledge of the delays and do not perform well for small model uncertainties. Adaptive algorithms have been developed by Ioannou et al., [11], to address unpredictable changes in brake model parameters. Recent work by Maciuca and Hedrick, [15], shows that non smooth estimation and adaptation techniques can be used to achieve satisfactory brake torque control under uncertainties and modeling errors. We will mainly focus on online adaptation of PI and PIQ controller gains based on parameter estimation using the speed gradient methodology.

4) Experimental Implementation (anticipated):

Our algorithms will be implemented and tested on a Freightliner CHV donated by the Freightliner Corporation. Moreover, it is anticipated that our control algorithms will be selected for the 2002 Federal Highway Administration demonstration of automated and semi-automated CVH operation.

The experimental CHV is powered by a 350 Hp Detroit Diesel DDEC III engine, and equipped with: turbocharger, intercooler, a 6-speed automatic Heavy-Duty World Transmission, an electronic service brake system, steering by wire, a driveline retarder, and a compression brake. The tractor is connected with a Great Dane 45 feet semitrailer. Hence, the total vehicle system is about 20 meter long, about 4 meter high; it has 18 wheels and maximum mass of about 36,500 kg.

The challenging experimental aspects of the control implementation involve measuring shaft torque in a vehicle application, and characterization of the interaction between longitudinal and lateral control. Coordinating braking control with steering control to eliminate jack-knifing (the large unwanted yaw motion between the truck and the trailer) can be pursued as an extension of the work by Chen and Tomizuka, [3].

10 Acknowledgments

The work is supported in part by the California Partners for Advanced Transit and Highways (PATH) under MOU 372, and Mack Trucks, Inc. Joseph Schmidt from Mack Trucks is our industrial advisor and collaborator.

References

[1] BD. "Exhaust Brake". Retrieved on: http://www.bd-vfi.com/Exhaust_Brakes/Turbo_Mount_Exhaust_Brake/, September 1999.

[2] P. Carlstrom. "Volvo High Power Engine Brake". Retrieved on: http:/www.truck.volvo.se, May 1999.

[3] C. Chen and M. Tomizuka. "Steering and Independent Braking Control for Tractor-Semitrailer Vehicles in Automated Highway Systems". In *Proceedings for CDC"*, 1995.

[4] D. D. Cummins. "The Jacobs Engine Brake Application and Performance". *SAE*, (660740), 1966.

[5] Daimler-Chrysler. "Hybrid Electric Vehicle". Matlab News Bulletin, 1999.

[6] J. W. Fitch. *Motor Truck Engineering Handbook*. SAE, Inc., 4th. edition, 1994.

[7] C. J. Gerdes, S. A. Brown, and K. J. Hedrick. "Brake System Modeling for Vehicle Control". *Advanced Automotive Technologies*, pages 105–112, 1995.

[8] J. B. Heywood. *Internal Combustion Engine Fundamentals*. McGraw-Hill, 1988.

[9] H. Hu, M. A. Israel, and J. M. Vorih. "Variable Valve Actuation and Diesel Engine Retarding Performance". *SAE*, (970342), 1997.

[10] H. Hu, J. Vorih, and M. Israel. "Lost-Motion VVT Diesel Engine Retarder". *Automotive Engineering International*, Jan, 1998.

[11] P. Ioannou and Z. Xu. "Throttle Control for Vehicle Following", 1993.

[12] M. A. Israel and H. Hu. "Impact of Ambient Parameter on Operating Efficiency of Compression Release Engine Retarder Systems on Heavy Duty Diesel Engines". *SAE*, (932972), 1993.

[13] John Deere. "Sharing the Road Media Group". Retrieved on: http://www.deere.com/truckerimage/sharing.

[14] I. Kanellapooulos. "Integrated Longitudinal Control for Safe Automation of Commercial Heavy Vehicles". Proposal for the awarded MOU 393, 1999.

[15] D. B. Maciuca and K. J. Heidrick. "Nonsmooth Estimation and Adaptive Control with Application to Automotive Brake Torque". In *Proceedings for ACC*, 1998.

[16] L. Moklegaard, J. Schmidt, and A. G. Stefanopoulou. "Transition from Combustion to Variable Compression Braking". In *future Proceedings for the 2000 SAE World Congress"*, 2000.

[17] J. M. Novak. "Simulation of the Breathing Process and Air-Fuel Ratio Distribution Characteristics of Three-Valve, Stratified Charge Engines". *SAE*, (770881), 1977.

[18] H. Raza, Z. Xu, and B. Yang. Brake Modeling for AVCS Application. Technical Report 94-01-01, PATH, 1994.

[19] W. B. Ribbens. *Understanding Automotive Electronics.* SAMS, 4th. edition, 1992.

[20] D. E. Seborg, T. F. Edgar, and D. A. Mellichamp. *Process Dynamics and Control.* John Wiley & Sons, Inc., 1989.

[21] J. E. Shigley and J. J. Uicker. *Theory of Machines and Mechanisms.* McGraw-Hill, 2nd. edition, 1995.

[22] S. E. Shladover and other. "Automatic Vehicle Control Developments in the PATH Program". *IEEE Trans. on Vehicular Technology*, 40(1):114–130, 1991.

[23] S. Skogestad and I. Postlethwaite. *Multivariable Feedback Control Analysis and Design.* John Wiley & Sons, 1996.

[24] Jacobs Vehicle System. "Intebrake Engine Braking Systme for Signature 600". Retrieved on: http:/www.jakebrake.com/products/engine, March 1999.

[25] Jacobs Vehicle Systems. "Driveline Brakes". Retrieved on: http://www.jakebrake.com/, Nov 1999.

[26] D. Yanakiev, J. Eyre, and I. Kanellakopoulos. "Longitudinal Control of Heavy Vehicles with Air Brake Actuation Delays". In *Proceedings for ACC"*, 1997.

[27] D. Yanakiev, J. Eyre, and I Kanellakopoulos. "Longitudinal Control of Automated CHV's with Significant Actuator Delays". Technical Report UCB-ITS_PRR-98-15, PATH, 1998.

[28] D. Yanakiev and I. Kanellakopoulos. "Engine and Transmission Modeling". California PATH Technical Note 95-6, 1995.

[29] D. Yanakiev and I. Kanellakopoulos. "Longitudinal Control of Automated CHV's with Significant Actuator Delays". In *Proceedings for CDC"*, 1997.